



Contents lists available at ScienceDirect

International Journal of Rock Mechanics and Mining Sciences

journal homepage: www.elsevier.com/locate/ijmms

Mechanical anisotropy of coal under coupled biaxial static and dynamic loads

J. Li^a, J. Zhao^a, S.Y. Gong^b, H.C. Wang^a, M.H. Ju^{a,c}, K. Du^d, Q.B. Zhang^{a,*}

^a Department of Civil Engineering, Monash University, VIC, 3800, Australia

^b Laboratory of Mine Earthquake Monitoring and Prevention, School of Mines, China University of Mining & Technology, Xuzhou, Jiangsu, 221116, PR China

^c State Key Laboratory for Geomechanics & Deep Underground Engineering, China University of Mining & Technology, Xuzhou, Jiangsu, 221116, PR China

^d School of Resources and Safety Engineering, Central South University, Changsha, Hunan, 410083, PR China

ARTICLE INFO

Keywords:

Triaxial hopkinson bar
Coupled static and dynamic loading
Coal burst
Anisotropy
Dynamic hazards

ABSTRACT

Understanding the mechanical properties and fracturing behaviours of coal is significant for the safety of underground mining engineering. Coal failure characteristics are highly influenced by the anisotropy and loading conditions. In this study, the coupled biaxial static and dynamic tests are conducted on coal specimens with five bedding orientations θ (i.e., 0°, 30°, 45°, 60°, and 90°) with respect to the normal direction to loading. A Triaxial Hopkinson bar (Tri-HB) system is adopted to apply the biaxial quasi-static stress first and then dynamic loading at four impact velocities (i.e., 10, 13, 17, and 21 m/s). Real-time processes of coal fracturing are recorded by two high-speed cameras, and accordingly, full-field deformation and ejection velocities are identified by the three-dimensional digital image correlation (3D-DIC) technique. Moreover, the internal fracture morphology of coal specimens is characterised using synchrotron-based X-ray computed tomography (CT). Experimental results show that at similar strain rates, the peak stress against θ shows a “U” shape with the lowest value at $\theta = 60^\circ$. The peak stress increases with increasing impact velocity, while its growth rate exhibits a downward trend revealing a decreasing sensitivity to strain rate. Coal ejection velocities are positively rate-dependent, and the highest ejection velocity is found shifting from $\theta = 45^\circ$ to $\theta = 90^\circ$ with increasing impact velocity. The average fragment size of coal specimens is negatively related to impact velocities and energy absorption, and the finest fragmentations are observed at around $\theta = 45^\circ$. Dynamic behaviours of coal under biaxial pre-stresses are dependent on bedding structures and strain rates, while the bedding effect becomes weak as strain rate increases.

1. Introduction

The rockburst, as a particular seismic event, poses a persistent threat to the safety of underground excavations.^{1,2} It involves the ejection of rock fragments at high velocity from the surfaces of the cavern, which is highly likely to result in fatal mining accidents.^{3–5} Rockburst is also a severe disaster in underground coal mining engineering, which results from a violent release of energy expelling coal mass into mining faces or roadways.^{6,7} In this study, the term “coal burst” is adopted to indicate rockburst particularly occurring in coal mines. Coal bursts have led to a huge number of economic losses and casualties around the world. For example, a coal burst accident in Springhill Coal Mine in Nova Scotia, Canada, claimed 75 lives.⁸ Most recently, a coal burst in Longyan Coal Mine in Yancheng City, China, trapped 22 miners and caused ten fatalities on 20 October 2018.⁹ Moreover, numerous field and

experimental cases show that the severity of coal bursts is much greater than rock bursts, which is most likely due to the unique behaviour of coal and excavation methods. For example, rock bursts usually only cause a small range of rock failures¹⁰; however, an intense coal burst can destroy roadways up to several hundred meters in length.^{11,12} It was reported that the ejection velocity of fragments in a rockburst was normally below 10 m/s,^{13–17} but that in a coal burst could be up to 20 m/s.^{18,19} The coal burst becomes progressively severe with the increase of mining depth and complex geological conditions. Hence, to guarantee coal mining safety, it is imperative to understand the mechanism of coal bursts.

The complex *in-situ* stress environment is one of the main factors to dominate coal bursts. Coal masses may suddenly fail when subjected to high stresses induced by the movement of geological discontinuities (e.g., faults, dykes and folds)^{20–22} and mining activities (e.g., mine design

* Corresponding author.

E-mail address: qianbing.zhang@monash.edu (Q.B. Zhang).

<https://doi.org/10.1016/j.ijmms.2021.104807>

Received 6 July 2020; Received in revised form 22 April 2021; Accepted 3 May 2021
1365-1609/© 2021 Elsevier Ltd. All rights reserved.

parameters and mining practices).^{23,24} During the mining process, coal bursts can be triggered by various dynamic/seismic loads from fault slip,²⁵ roof collapse^{26,27} and blasting.²⁸ Experimental tests play a vital role in understanding the mechanism of coal bursts owing to the conveniently controllable conditions. Various theories and criteria were proposed to evaluate the rockburst proneness based on uniaxial,^{29–33} biaxial^{34,35} and triaxial tests.^{36,37} For example, a modified true triaxial apparatus was developed by He et al. (2010)³⁸ to simulate *in-situ* unloading-induced rockbursts. The setup configuration can simulate rockbursts occurring in the near-face region after underground excavation. It was further adopted to investigate the effect of specimen size,³⁹ rock lithology^{40,41} and bedding plane orientations⁴² on rockbursts associated with unloading. Valuable findings have been achieved to underpin the mechanisms of coal bursts under static stress conditions. However, rockbursts induced by dynamic loading are inadequately understood. Experimental studies on dynamic-induced rockbursts were mainly simulated by applying either locally frequent dynamic-disturbance or high-amplitude impact loading. The former was achieved by true-triaxial dynamic-static loading testing apparatus,^{43–45} while the modified Hopkinson bar system was applied for the latter.^{46–49} Experimental studies showed that the strength, failure modes and energy evolution of rock under dynamic loading conditions are substantially different from those under quasi-static conditions.^{50–52} The existing studies mainly focus on the dynamic-induced rockbursts under uniaxial or unloading conditions, which is applicable to simulate coal bursts in pillars and longwall faces. However, the stress conditions of underground mining are mostly not in the uniaxial state, and around 53% of the coal bursts in Chinese coal mines occurred in roadways (multiaxial stress).²³ Also, more dynamic-induced coal bursts were reported in these locations.¹² Thus, it is indeed crucial to investigate the effect of dynamic loads on coal bursts under multiaxial stress conditions.^{49,53,54}

In addition to stress conditions, coal bursts are heavily affected by the physical and mechanical properties of coal itself, including unique bedding structures and complex pore and cleat systems, which highly increases the prediction uncertainty in coal failures.⁵⁵ Among them, beddings are regarded as the dominant factor influencing strength, deformation and failure modes of layered rocks.^{56–60} The existence of bedding planes has a great impact on coal/rock bursts based on laboratory experiments,^{42,61,62} numerical simulations^{63,64} and field observations.^{3,65–67} Great achievements have been made to explore the effect of bedding planes on the tendency, severity and mechanisms of coal/rock bursts. For example, rockbursts are controlled by the strength and structural stability when the bedding planes were perpendicular and parallel to the unloading surface, respectively.⁴² Rockbursts types can be changed from fault-slip, shear rupture to buckling with changes of weak plane orientations.⁶¹ The shape of ejected blocks is determined by the bedding separations, and higher densities of bedding planes lead to larger volumes of ejected bodies.⁶⁸ The ejection velocity and released kinetic energy of failed rocks are much higher in tunnels with bedding planes.⁶⁹ The bursting behaviour of coal with bedding planes parallel or perpendicular to the direction of dynamic loads is higher than that with oblique bedding planes, which is primarily controlled by the higher storage capacities of elastic strain energy in the former case.⁶³ It has also been found that the dynamic load contributes significantly to coal bursts in roadways and its contribution varies with different bedding plane angles associated with coal seams.^{70,71} However, to the best of our knowledge, the effect of bedding planes on rockbursts under coupled biaxial static and dynamic loading conditions has not yet been fully studied, which is of critical knowledge for the design of roadway supports during coal mining.

This paper is to systematically investigate coal bursts under coupled biaxial static and dynamic loading conditions using a Triaxial Hopkinson bar (Tri-HB) system with a specific emphasis on the effect of anisotropic bedding planes. Dynamic mechanical behaviours, including stress-strain curves and peak stresses, are analysed under a series of

impact velocities. The high-speed three-dimensional digital image correlation (3D-DIC) technique is adopted to record real-time deformation and bursting process of coal specimens. Moreover, internal fracture morphologies of some typical coal specimens are conducted by using the synchrotron-based X-ray CT. Coal fragmentation and energy characteristics are also analysed to understand dynamic failure features.

2. Materials and experimental methods

2.1. Coal specimens

Coal specimens tested in this study were selected from a longwall panel at an underground Coal Mine in Erdos City, Inner Mongolia, China. The average buried depth, thickness and inclination of the coal seam are 700 m, 4.8 m and 2°, respectively. The panel has been experiencing numerous mining-induced seismicities in the longwall retreat. At 00:59:51 CST, on April 8, 2018, a seismic event with an energy of 3.3×10^6 J detected by “SOS” microseismic monitoring system^{72,73} triggered a terrible coal burst on the tailgate of the panel, as shown in Fig. 1. This coal burst hazard caused tailgate damaged up to 762 m in length. The *in-situ* observation indicated that a large number of coal lumps was ejected out from the roadway surfaces, and mining equipment and support system were severely damaged after the coal burst. It is analysed that this strong seismicity that induced the hazard resulted from the sudden collapse of the hard roof 71 m above the mining coal seam.⁷⁴

Coal specimens were taken from the working face near the coal burst damage regions. Coal rank is identified as bituminous (middle rank) with maximum vitrinite reflectance ($R_{o,max}$) of 0.56%. The moisture content (2.63%), ash (13.65%), volatile matter (35.18%) and fixed carbon (55.97%) were determined by proximate analysis.⁷⁵ Coal petrographers are characterised by high inertinite content (78.47%), moderate vitrinite content (20.86%), and small amounts of liptinite (0.67%). The density of the prepared coal specimen is 1.35 g/cm³. The surface morphologies of the coal specimen were verified at Monash Centre for Electron Microscopy. Fig. 2 shows the Scanning Electron Microscope (SEM) images taken parallel and perpendicular to coal beddings. It can be seen that the formation of coal macerals has obvious directionality (bedding planes) due to the sedimentation effect, and abundant pores were generated in macerals. Minerals were also detected in SEM images, as demonstrated in Fig. 2(c), which were identified mainly as calcite by SEM-EDS (Energy Dispersive Spectrometer). Calcites were also examined by reflected light microscopy with the oil-immersion lens, showing that they are distributed along the bedding planes, as shown in Fig. 2(d).

Standard cubic specimens with a size of $50 \times 50 \times 50$ mm³ were cut and polished from large coal blocks. Three opposite pairs of faces were ground to parallel with the accuracy of ± 0.05 mm, and each adjacent surface is perpendicular to each other with a maximum deviation of 0.25°. The specimen was processed into a cube so that it can be loaded biaxially using triaxial systems. Five groups of bedding orientations θ (namely, 0°, 30°, 45°, 60° and 90°) were considered in the biaxial tests, where θ is the angle between bedding planes and the normal of axial load (σ_1). The lateral load (σ_2) is loaded parallel to bedding planes, as shown in Fig. 3. The mechanical properties of coal specimens with bedding orientation $\theta = 0^\circ, 30^\circ, 45^\circ, 60^\circ$ and 90° are as follows: uniaxial compressive strength $\sigma_c = 27.16, 19.44, 15.95, 15.47$ and 22.85 MPa; Elastic modulus $E = 2.17, 1.78, 1.67, 1.64$ and 2.46 GPa; P-wave velocity $C_p = 1762, 1902, 1973, 2080$ and 2385 m/s; and S-wave velocity $C_s = 995, 1015, 1026, 1082$ and 1018 m/s, respectively.

2.2. Quasi-static and dynamic biaxial testing procedures

Quasi-static biaxial tests were conducted using a true-triaxial loading testing apparatus in Central South University, China. The detailed introduction of the loading system can be found in Refs. 45,76–78. The purpose of quasi-static biaxial tests is to examine the effect of

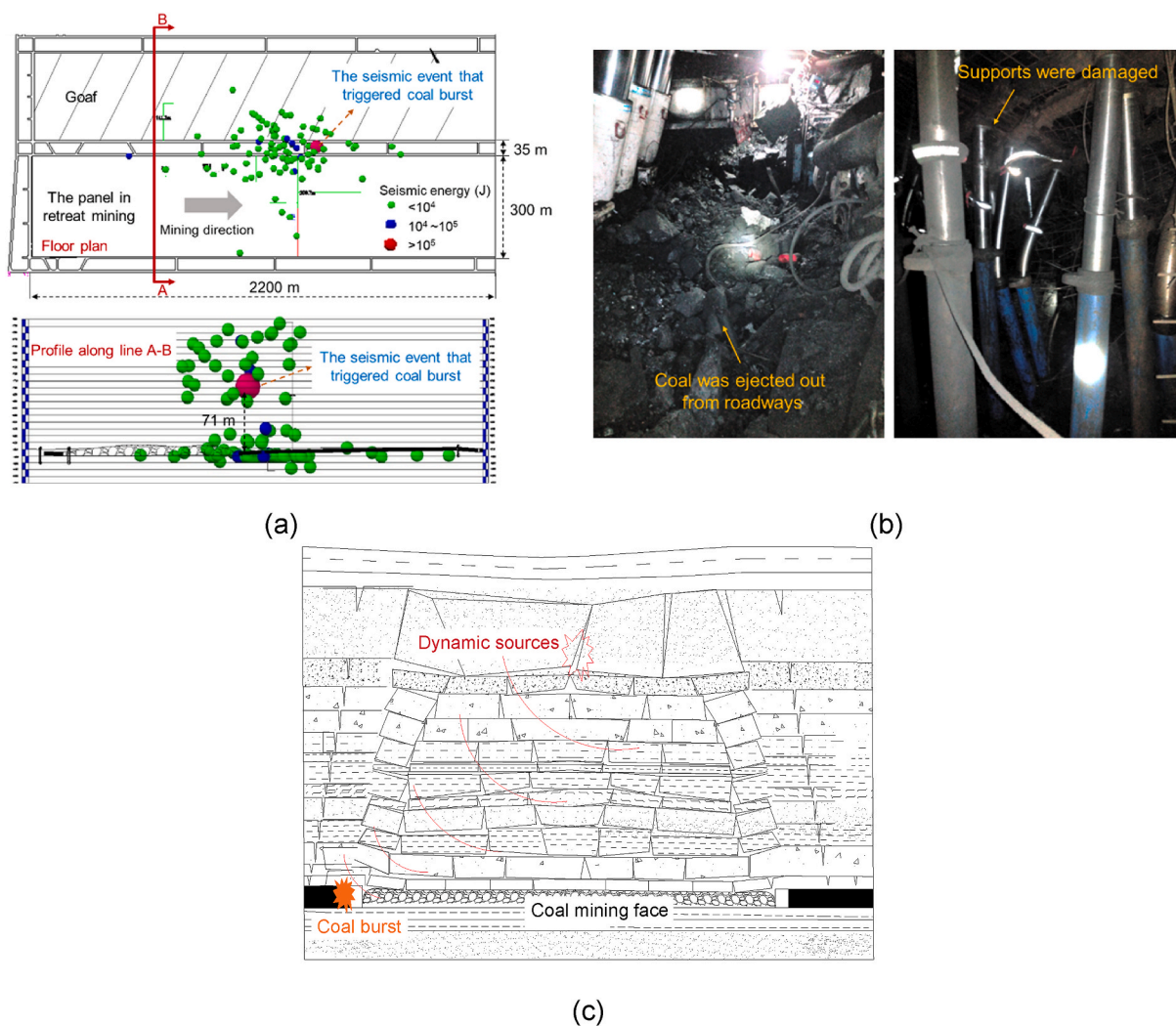


Fig. 1. A coal burst induced by a dynamic loading: (a) microseismic events recorded during coal mining process; (b) roadway damage after the hazard; (c) schematic of the mechanism of dynamic-loading induced coal bursts.

confinements on coal failure characteristics. $\sigma_1 = 10$ MPa and $\sigma_2 = 5$ MPa are specially chosen in this study to simulate the *in-situ* stress conditions to the greatest extent and meanwhile to guarantee that the selected pre-stresses can be successfully loaded on coal specimens with any bedding angles. A typical bedding orientation $\theta = 0^\circ$ was selected to examine the confinement effect. In biaxial tests, the axial (σ_1) and lateral (σ_2) loads were first applied to reach the same stress level (5 MPa). Then, σ_2 kept constant at the predefined value, and σ_1 was monotonically increased at the loading rate of 0.15 mm/min until the specimen failure. The uniaxial tests were also conducted for comparison, and axial stress σ_1 was applied at the loading rate of 0.15 mm/min.^{77,78} The testing results were shown in Fig. 4. It can be seen that the confinement has a great influence on the failure strength and failure modes: under biaxial confinement, the coal specimen is characterised by high strength and multiple tensile cracks parallel to σ_2 direction.

After examining the confinement effect, coupled biaxial static and dynamic loading tests were conducted using the Tri-HB system, as shown in Fig. 5(a). The system has three independent pairs of steel square bars (42CrMo Steel, cross-section 50×50 mm²) which are aligned orthogonally in X, Y and Z directions. The mechanical properties of the bars are: density $\rho_b = 7850$ kg/m³, Young's modulus $E_b = 210$ GPa and longitudinal wave velocity $C_L = 5200$ m/s. Among three pairs of bars, there is a loading cell for placing a standard cubic specimen of $50 \times 50 \times 50$ mm³ as shown in Fig. 5(b). Three hydraulic cylinders

(pressure capacity up to 100 MPa) can move the steel bar to apply different pre-stresses on the specimen in three perpendicular directions. The dynamic loading was applied in the X-axis by the launch of the striker (42CrMo Steel, length 0.5 m, diameter 40 mm) compressed by the gas gun. When the striker hits the incident bar (2.5 m), a compressive stress wave will be generated and propagate towards the specimen. Since the difference of impedances between bars and specimen, a reflection wave will be generated on the contact surface of the incident bar, and a transmission wave will also be generated into the transmission bar (2 m). Meanwhile, the output wave will also propagate in the Y and Z bars (2 m). Red copper discs (diameter 15 mm, thickness 1.5 mm) are served as pulse shapers to produce a ramped incident wave that reduces high-frequency oscillations and minimise the dispersion effect. Strain gauges (FLA-6-11) are attached on the bars to record strains, and these signals will be digitised to 12 bits at a 1 MHz sampling frequency by an analogue-to-digital converter-NI PXIe 5105. The velocity of the striker bar is measured by a laser-beam velocity measurement system. The detailed introduction of the Tri-HB system can be referred to the previous publications.^{49,53,54}

In this study, the coal specimen was subjected to dynamic loading with biaxial pre-stress conditions. Biaxial pre-stresses σ_1 and σ_2 were applied on the specimens in the X and Y directions, respectively. The dynamic loadings were applied along the direction of σ_1 . The experimental procedures are as follows: (1) the specimen is placed between

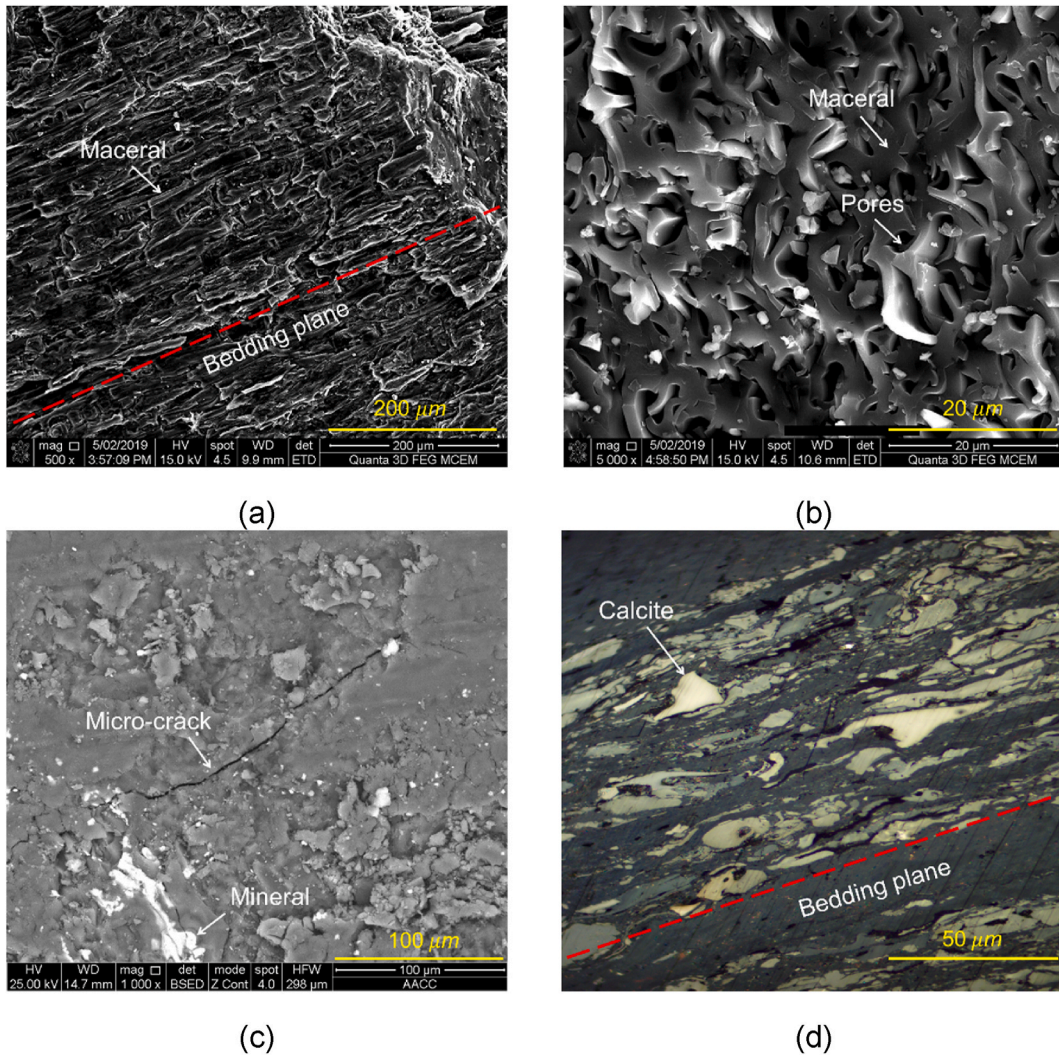


Fig. 2. Petrographic images of the coal: (a) SEM images taken parallel to coal beddings and (b) perpendicular to coal beddings; (c) minerals observed in the SEM image; (d) calcite distributed parallel to the bedding by the optical microscope.

bars in the loading cell; (2) desired pre-stresses $\sigma_1 = 10$ MPa in X direction and $\sigma_2 = 5$ MPa in Y direction are applied to the specimen by hydraulic cylinders with a low loading rate $\sim 10^{-4}$ GPa/s; (3) nitrogen in the gas cylinder is injected into the gas gun for desired gas pressure; (4) gas pressure is released to drive striker impacting the incident bar in the X direction with impact velocities (V_i) of 10, 13, 17 and 21 m/s corresponding to approximately 80, 130, 190 and 250 s^{-1} of strain rates; (5) impact velocity and strain histories were recorded by the data acquisition system; and (6) after each test, coal debris was carefully collected from the loading cell for further fragmentation analysis.

The dynamic stress σ , strain rate $\dot{\epsilon}$ and strain ϵ in the specimen are obtained under the state of stress equilibrium⁴⁶:

$$\sigma_x(t) = \frac{E_b A_b}{2A_s} [\epsilon_{in}(t) + \epsilon_{re}(t) + \epsilon_{tr}(t)] = \frac{E_b A_b}{A_s} \epsilon_{ir}(t) \quad (1)$$

$$\dot{\epsilon}(t) = -\frac{2C_b}{L} \epsilon_{re}(t) \quad (2)$$

$$\epsilon(t) = -\frac{2C_b}{L} \int_0^t \epsilon_{re}(t) dt \quad (3)$$

where, σ_x is the dynamic stress along the X direction; E_b and A_b are Young's modulus, cross-sectional area of bars, respectively; A_s and L are

the cross-sectional area and the length of the specimen; ϵ is the strain measured by strain gauges on the bars. The subscripts 'in', 're' and 'tr' correspond to the incident, reflected and transmission waves in the impact direction, respectively. The respective stress and strain of the specimen in the Y direction can be calculated by^{49,53,54,79}:

$$\sigma_y(t) = \frac{E_b A_b}{2A_s} [\epsilon_{y1}(t) + \epsilon_{y2}(t)] \quad (4)$$

$$\epsilon_y(t) = \frac{C_b}{L} \int_0^t [\epsilon_{y1}(t) + \epsilon_{y2}(t)] dt \quad (5)$$

The absorbed energy of rock specimen under dynamic loads can be calculated as follows^{53,80}:

$$W_s = W_0 + W_{in} - W_{re} - W_{tr} - W_{y1} - W_{y2} \quad (6)$$

where W_s is the energy absorbed by coal specimen; W_0 is strain energy stored in the coal specimens during biaxial compressions, which can be expressed as:

$$W_0 = \frac{m}{2\rho} \sum \frac{\sigma_i^2}{E_i} \quad (7)$$

where m and ρ are mass and density of coal specimens; σ_i and E_i are

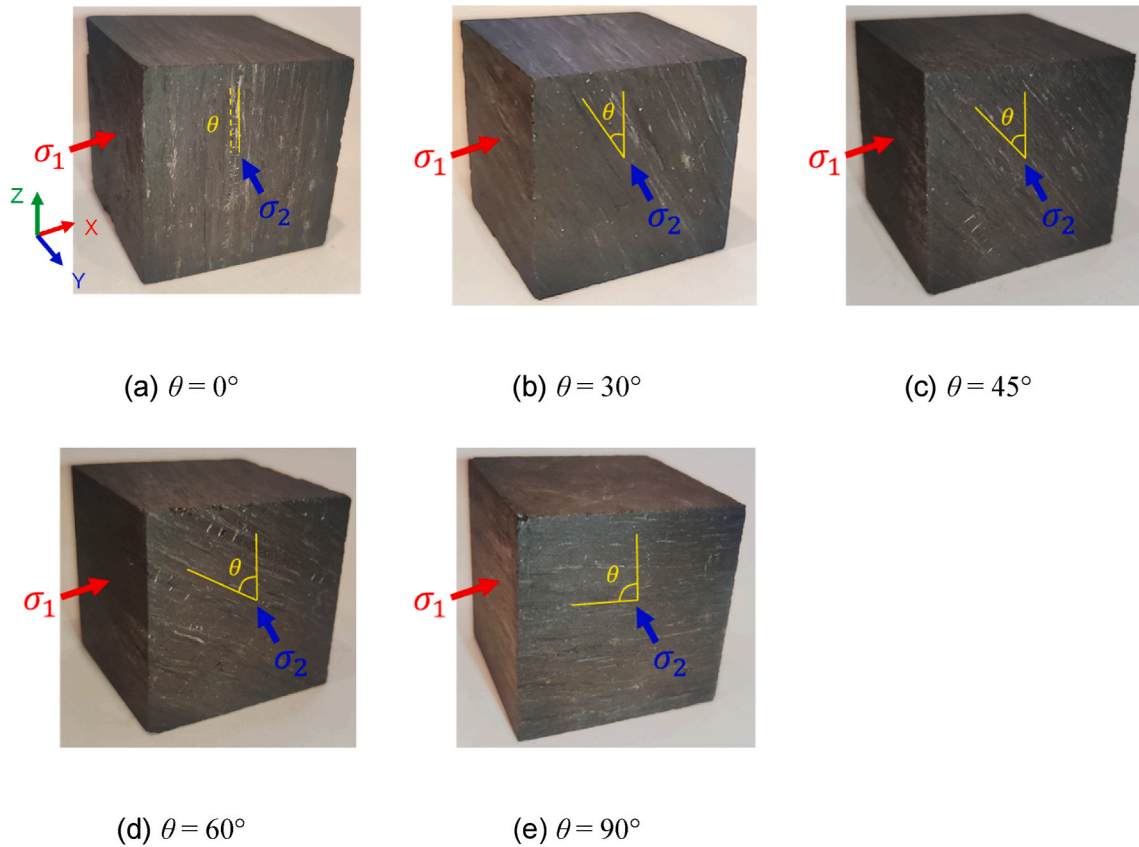


Fig. 3. Coal specimens with different bedding angles. σ_1 is the maximum stress in X-axis and σ_2 is the intermediate stresses in Y-axis.

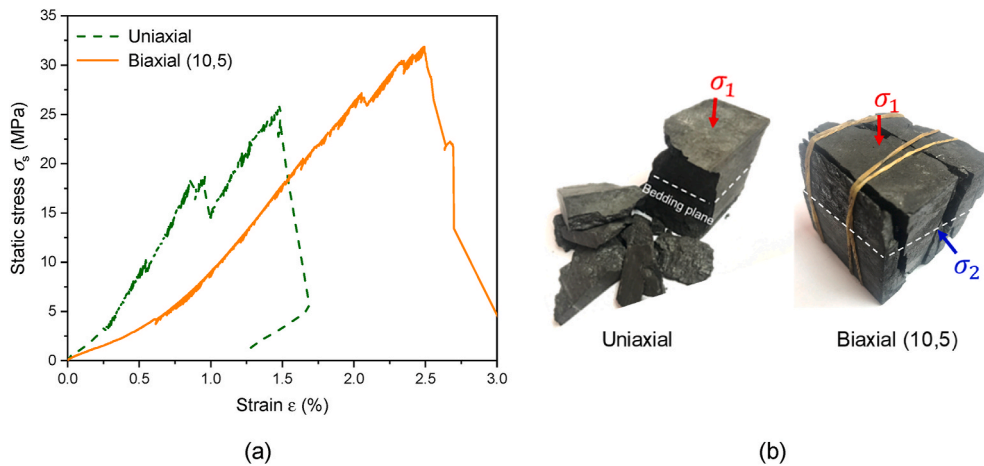


Fig. 4. Stress-strain responses of coal specimens at $\theta = 0^\circ$ in uniaxial and biaxial static tests (a) and corresponding failure modes (b). (10, 5) means the pre-stress combination of axial load $\sigma_1 = 10$ MPa and lateral load $\sigma_2 = 5$ MPa in the biaxial test, respectively.

principal pre-stresses applied on the coal and corresponding elastic modulus along the direction of principal stresses. W_{in} , W_{re} , and W_{tr} are energy carried by the incident, reflected, transmitted waves along the X direction, which can be calculated as follows:

$$W_{in} = \frac{A_b C_b}{E_b} \int \sigma_{in}(t)^2 dt \quad (8)$$

$$W_{re} = \frac{A_b C_b}{E_b} \int \sigma_{re}(t)^2 dt \quad (9)$$

$$W_{tr} = \frac{A_b C_b}{E_b} \int \sigma_{tr}(t)^2 dt \quad (10)$$

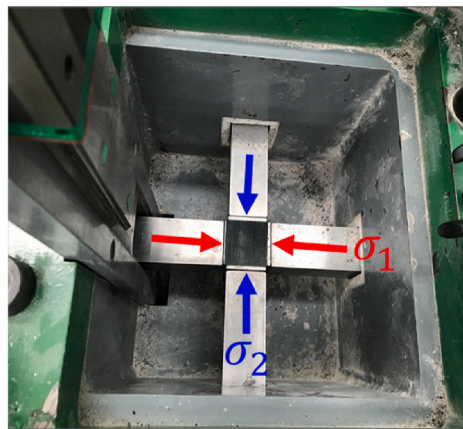
W_{y1} and W_{y2} are output strain energies along the Y-bar direction, which can be calculated by:

$$W_{y1} = \frac{A_b C_b}{E_b} \int \sigma_{y1}(t)^2 dt \quad (11)$$

$$W_{y2} = \frac{A_b C_b}{E_b} \int \sigma_{y2}(t)^2 dt \quad (12)$$



(a)



(b)

Fig. 5. Triaxial Hopkinson bar system at Monash University (a) and a standard cubic coal specimen placed between bars in the loading cell (b).

where $\sigma_{in}(t)$, $\sigma_{re}(t)$, $\sigma_{tr}(t)$ and $\sigma_y(t)$ are dynamic stresses for the incident, reflected and transmitted and Y-output bars, respectively.

2.3. High-speed imaging and 3D digital image correlation

The deformation fields and fracturing process of coal under the coupled biaxial static and dynamic loading condition were measured by the high-speed three-dimensional digital image correlation (3D-DIC) technique. A planar calibration target with regularly spaced circular dots is used to calibrate cameras to obtain their intrinsic parameters and extrinsic parameters. The detailed stereo-calibration process has been well described in various publications.^{81,82} Two high-speed CMOS cameras (Phantom V2511) mounted on tripods form a binocular vision system capturing grey-scale images of the specimen surface simultaneously from different views. A series of deformed images of coal specimen during impact is captured with the resolution of 256×256 pixels at 200,000 frames per second (fps). These camera parameters have been proven to be good in the high-speed 3D-DIC measurement of rocks in SHPB test.⁸³ Finally, these obtained calibration images and experimental images are processed to reconstruct the shape profile before and after deformation based on triangulation method.⁸⁴ The procedure to measure full-field shape profile and deformation using the

3D-DIC technique is schematically shown in Fig. 6.

3. Anisotropic mechanical and fracturing behaviour

3.1. Stress-strain curves and fracturing

With captured signals by strain gauges attached on the Tri-HB system, incident, reflected, transmitted waves in the impact direction and stress waves in Y-direction can be extracted. Fig. 7(a) presents typical experimental signals at the impact velocity of 17 m/s. In this study, compression is defined as positive since all of the pre-stresses and impacts are compressive. According to the International Society for Rock Mechanics (ISRM) suggested method,⁸⁵ the specimen should reach stress equilibrium before failure for a valid dynamic compression test. To meet this requirement, dynamic stresses on both ends of the specimen should be roughly identical. Fig. 7(b) illustrates the stress histories on both sides of the specimen along the impact direction in a typical coupled biaxial static and dynamic test. It is clear that the sum of incident and reflected stresses is basically equal to the transmitted stress; therefore, the uniformity of the dynamic stress across the specimen has been achieved. With dynamic stress balance, the stress-strain curve of coal specimens in the X and Y directions can be obtained from Eqs. (1)–(5).

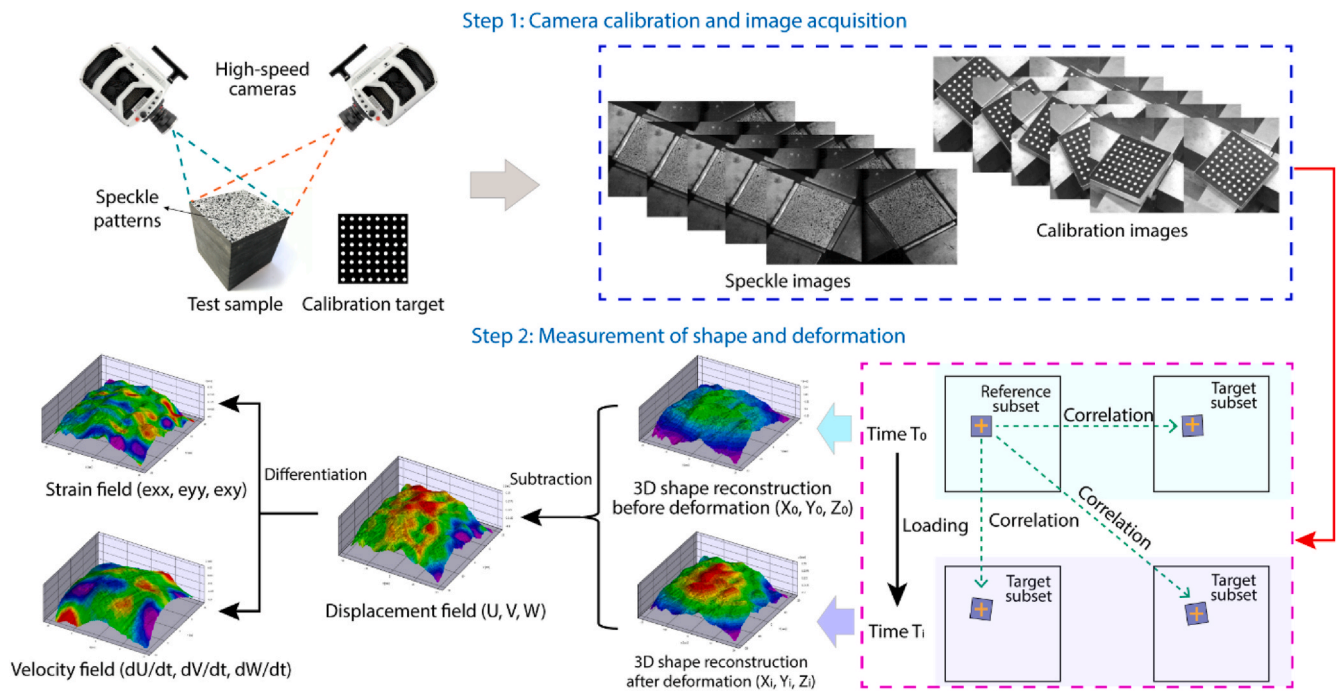


Fig. 6. The procedure to measure the shape profile and deformation using the 3D-DIC technique.

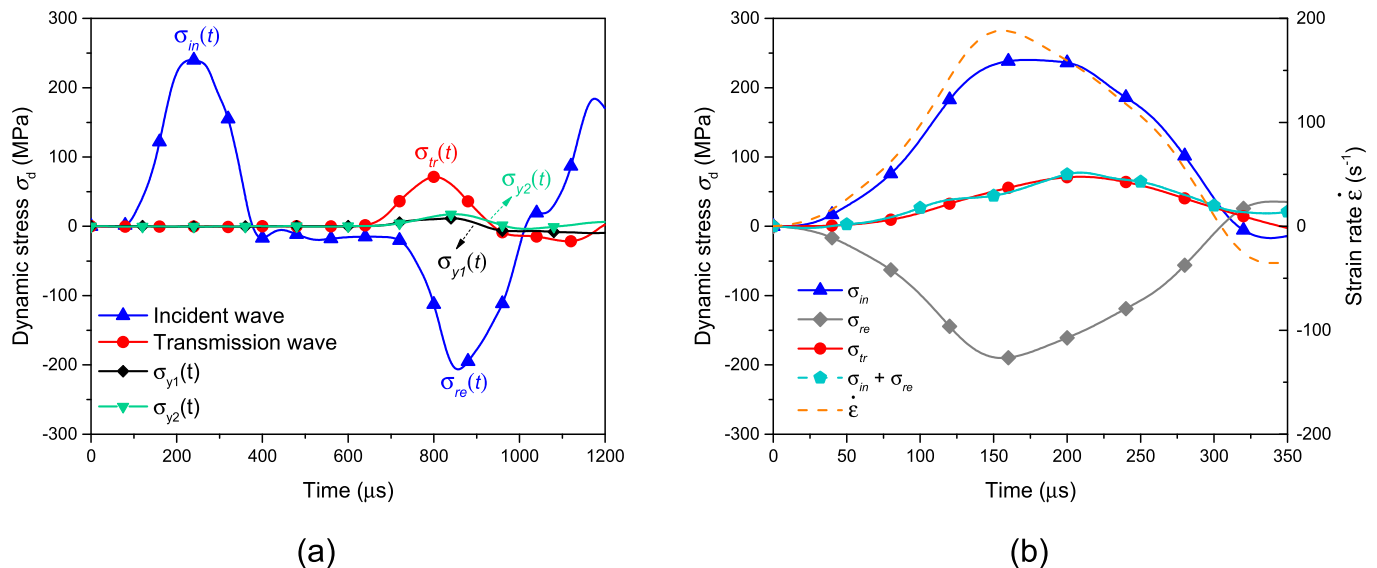
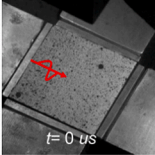
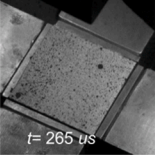
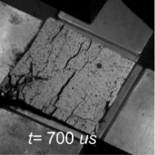
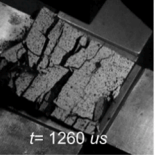
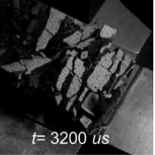
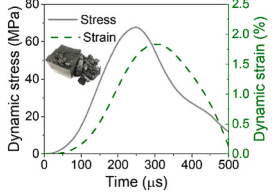
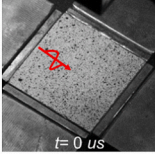
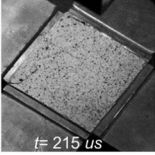
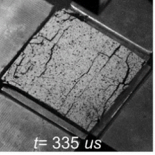
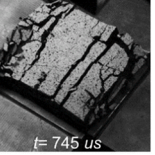
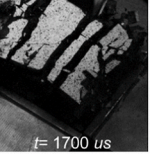
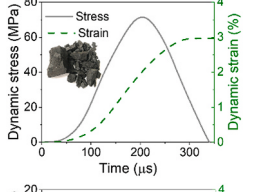
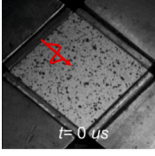
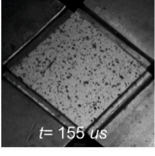
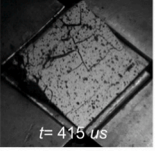
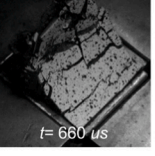
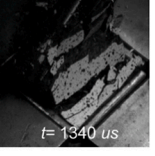
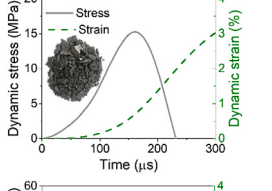
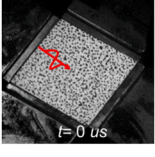
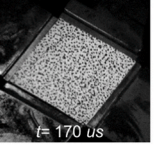
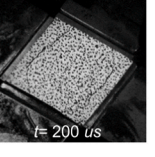
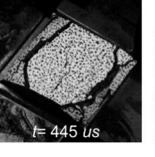
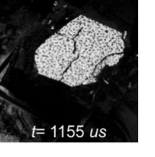
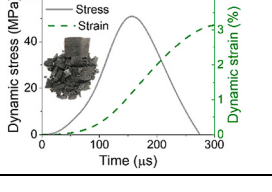


Fig. 7. Typical experimental data in the dynamic tests of coal specimens: (a) stress waves in X and Y directions; (b) dynamic stress equilibrium check along the impact direction.

Under coupled biaxial static and dynamic loading conditions, coal specimens deform elastically or slightly fractured at the low impact velocity. At the high impact velocity, specimens are broken into irregular fragments ejecting out from the exposed surface accompanied by a tremendous noise. Table 1 compares the typical high-speed images of coal bursting processes and corresponding histories of stress and strain. Fig. 8(a)–(e) depicts typical dynamic stress-strain curves during coal bursts reproduced in the laboratory tests for different bedding orientations. It can be seen that there is no obvious compaction stage at the beginning of dynamic stress-strain curves. Instead, coal specimens first experienced elastic deformation stage and then followed by nonlinear deformation until peak stress. After peak stress, stress-strain curves are classified into two types, *i.e.*, Class-I and Class-II curves, based on the features of residual strain.⁸⁶ For coal specimens at $\theta = 0^\circ$ and 90° ,

stress-strain curves gradually change from Class-I to Class-II type with increasing impact velocities, while only Class-II type can be found for coal specimens at $\theta = 30^\circ$, 45° and 60° . The dynamic strain of coal specimen with Class-I stress-strain curves firstly increases to the peak and then decreases, and the strain recovery in the unloading stage prevents further failure of specimens; thus, the coal specimen is not severely damaged and still has a certain bearing capacity. Generally, coal specimen with Class-I curves normally remain macroscopically intact or have a tensile split along the free surface. However, permanent deformation still occurs after unloading is completed due to the generation and propagation of microcracks during loading. The high-speed images of coal specimen with bedding angle $\theta = 0^\circ$ and $V_i = 13$ m/s in Table 1 present typical coal bursts with Class-I type. It can be observed that when applying dynamic compressive loading on coal specimens, a

Table 1
Coal failure processes under coupled biaxial static and dynamic loading conditions and corresponding history of stress and strain.

V_i (m/s)	$\theta(^{\circ})$	High-speed images of coal failure process					History of stress and strain
13	0						
17	0						
17	60						
17	90						

vertical displacement occurs in the Z direction due to the expansion effect. At the initial loading stage, the coal specimen deformed elastically without visible cracks on the surface. With further loading, some noticeable cracks perpendicular to impact direction emerge at the incident edge of coal specimen. They are tensile cracks attributed to the bending effect in the impact direction. Bent tension flakes coal specimen into small fragments along bedding planes where laminated layers are poorly connected with each other forming a weak link. Cracks develop to the transmitted edge, and finally, coal fragments are ejected out from the coal surface. The specimen in such loading case is not damaged, and its stress-strain curves belong to Class-I type as indicated in Fig. 8(a). The high-speed images of coal specimen with bedding angle $\theta = 0^{\circ}$ and $V_i = 17$ m/s in Table 1 present typical coal bursts with Class-II type. Coal failure processes in this stress-strain type are violent with the dynamic strain ϵ keeping increasing with loading time until specimen failure, and specimens are pulverised into many small fragments; additionally, the bearing capacity is greater than that in Class-I type.

Bedding planes have a great influence on the stress-strain response, as indicated in Fig. 8(f). At $V_i = 17$ m/s, Class-II stress-strain curves are derived for all bedding orientations indicating coal specimens have been damaged. The highest failure strength is observed at $\theta = 0^{\circ}$ followed by $\theta = 90^{\circ}$ and $\theta = 30^{\circ}$, while the lowest value is found at $\theta = 60^{\circ}$. Coal burst characteristics are also significantly affected by bedding angles, as shown in Table 1. Specifically, the 0° oriented coal specimen was separated into several flying fragments in bars along with the bedding directions. The common failure process of 60° oriented specimens is that the whole surface ejected out from the exposed surface, while the largest deformation occurs near the incident bar, and the flying fragments clearly rotate during coal bursting process. For specimens with the orientation of 90° , bent tension-induced cracks are observed near the incident and transmitter bars at 200 μ s, and finally, coal fragments fly out from the centre of the specimen surface.

3.2. Effect of bedding planes and strain rates on peak stresses

The peak stresses of coal specimens with different anisotropy angles θ and impact velocities V_i are plotted in Fig. 9. Peak stresses exhibit strong dependency on both θ and V_i . The curves of average peak stresses versus θ display a U-shaped form, as shown in Fig. 9(a), which is consistent with previous experimental results on the bedding rocks in quasi-static uniaxial and triaxial compression tests.⁸⁷ The maximum peak stress is observed at $\theta = 0^{\circ}$, while the minimum value is obtained at $\theta = 60^{\circ}$ throughout the range of all loading levels. Peak stresses are positively rate-dependent for all bedding angles, as demonstrated in Fig. 9(b). The most obvious strain rate effect on peak stresses is found at $\theta = 0^{\circ}$ showing 66.78% of peak stress increment when V_i increases from 10 to 21 m/s, while the peak stress increments are 33.2% and 19.9% at $\theta = 60^{\circ}$ and 90° , respectively. The effect of strain rates constantly slows down at a given bedding orientation. Fig. 9(c) and (d) present all experimental data and normalised data of peak stresses in the present work, respectively. It can be found that peak stresses have a linear dependence on the logarithm of strain rates, but the effect of strain rates on peak stresses is anisotropic. Coal specimens with bedding orientations in the range of 0° – 45° are more sensitive to strain rates since slopes of the fitting lines at these angles are much steeper. The gentle slopes of the fitting lines indicate that specimens with bedding orientations from 60° to 90° have low strain-rate sensitivity.

A strength anisotropy index (R_c) was introduced to describe the anisotropic behaviour of oriented coal specimens, which is defined as follows⁸⁸:

$$R_c = \sigma_0 / \sigma_{min} \tag{15}$$

where, σ_{min} is the minimum strength obtained from oriented specimens, and σ_0 is strength at $\theta = 0^{\circ}$. In this study, the anisotropy index $R_c = \sigma_0 / \sigma_{60^{\circ}}$ is 2.82, 3.63, 3.76 and 3.53 at impact velocities of 10, 13, 17 and 21 m/s, respectively. It indicates that the anisotropy index first increases

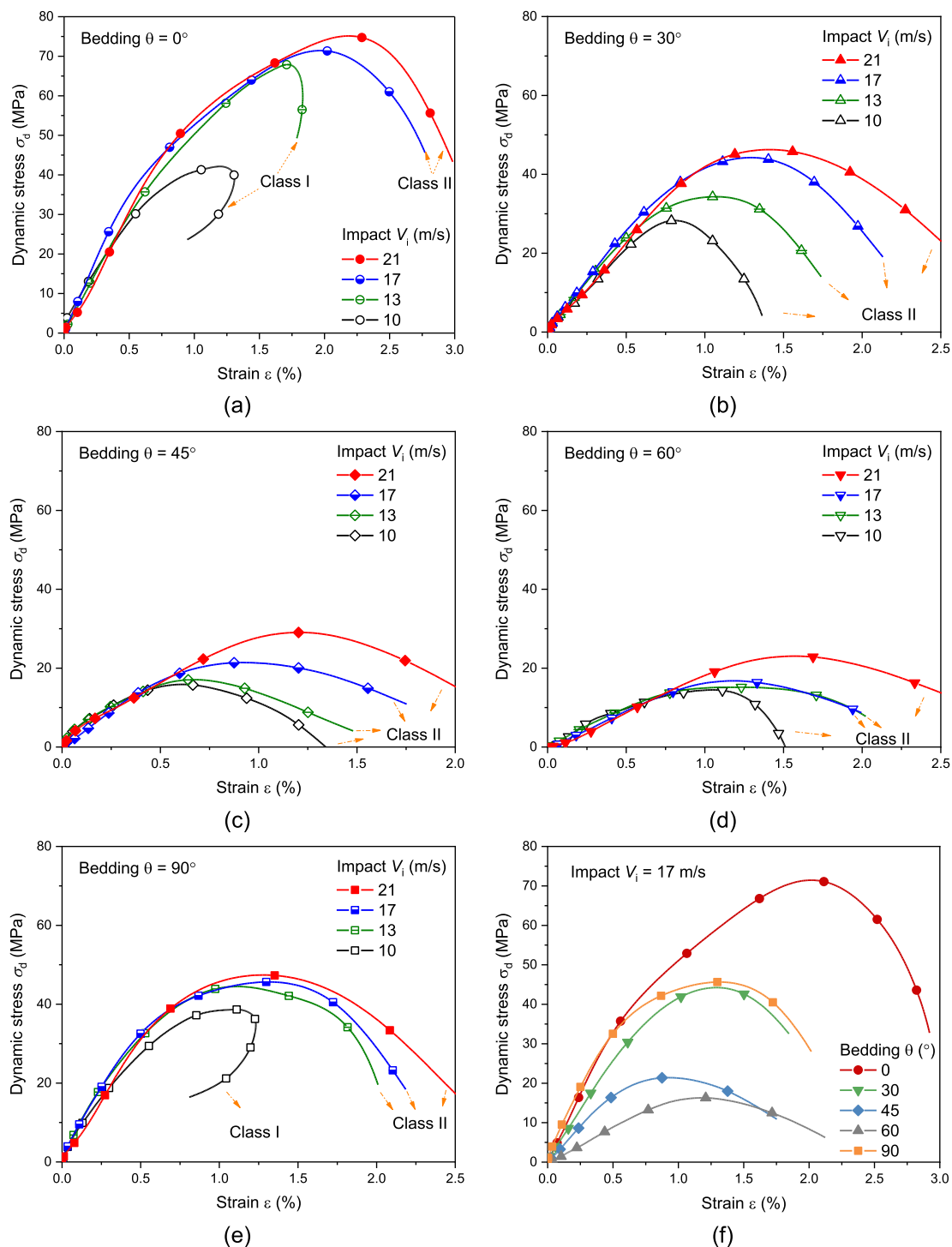


Fig. 8. Typical dynamic stress-strain curves of coal specimen under biaxial pre-stress states: (a-e) effect of impact velocities for different bedding angles; (f) effect of bedding angles at the impact velocity of 17 m/s.

and then decreases with increasing impact velocities. Peak stresses of coal specimens at $\theta = 0^\circ$ and $\theta = 60^\circ$ both show rising trends with impact velocities growing. However, coal specimens at $\theta = 0^\circ$ show more sensitivity to the strain rates than those at $\theta = 60^\circ$, especially when V_i is from 10 to 13 m/s (Fig. 9(b)). This leads to an increase in $\sigma_{0^\circ} / \sigma_{60^\circ}$. On the other hand, the rate sensitivity for $\theta = 0^\circ$ declines with the strain rate raising, which is shown as the decrease of strength increment. Therefore, $\sigma_{0^\circ} / \sigma_{60^\circ}$ also shows a slow growth trend, and the peak value is found at $V_i = 17$ m/s. In this regard, the strength anisotropy is mainly controlled by the bedding structure when V_i is from 10 to 17 m/s. At $V_i > 17$ m/s,

the dependence of the coal strength at $\theta = 0^\circ$ on the strain rates rapidly weakens, resulting in a decrease of $\sigma_{0^\circ} / \sigma_{60^\circ}$. This leads to a reducing trend in the strength anisotropy index at the high impact velocities. Consequently, the contribution of the bedding effect to strength anisotropy decreases and anisotropic strength behaviour is mainly affected by strain rates.

3.3. Full-field measurement of coal bursting

By processing deformed and reference images, X-, Y-, Z-directional

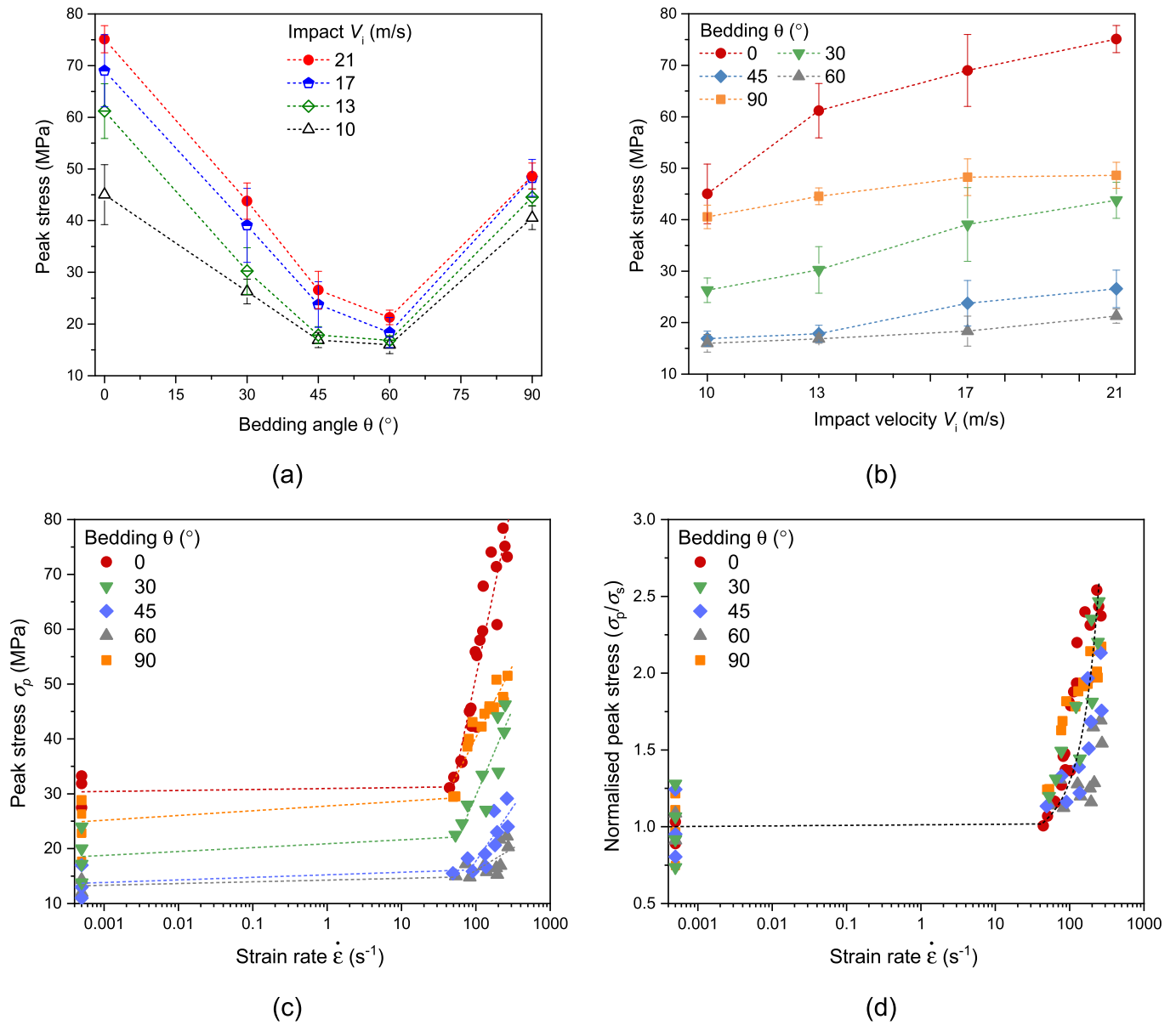


Fig. 9. Dynamic peak stresses against anisotropic angles (a) and impact velocities (b), and experimental data (c) and normalised data (d) in this work. σ_s means the peak stress under static loading conditions.

displacement fields u , v and w can be obtained during coal bursting processes using the established DIC system (Fig. 6). These displacement fields are calculated at a square of 36 mm on the exposed coal surface with a subset size 31×31 pixels. Table 2 shows typical measured w -displacement responses of coal specimens under different impact velocities and bedding orientations. The w -displacement profile along line AB (impact direction) is also extracted and plotted in Table 2. For $\theta = 0^\circ$, the deformation in Z-direction increases slowly at the initial loading stage when $V_i = 13$ m/s. Subsequently, the coal specimen begins to deform rapidly after 150 μ s, and the maximum deformation is shifted from the middle of the specimen to the incident edge at 250 μ s. When V_i is raised to 17 m/s, the distribution of w -displacement field is similar to that at $V_i = 13$ m/s, but the average displacement of the former is higher than the latter. For $\theta = 60^\circ$, the out-of-plane deformation first occurs in the incident edge of the coal specimen after which the maximum deformation is always observed there. Furthermore, the maximum displacement of coal specimens with this orientation at 250 μ s is almost twice as many as that of specimens at $\theta = 0^\circ$ at the same impact velocity. For $\theta = 90^\circ$, the entire surface of the specimen is continuously translated

upward during the whole loading process, which is consistent with high-speed images of coal failure process in Table 1. The possible explanation is that the 90° oriented specimens have a strong tendency for undergoing splitting parallel to beddings which are poorly connected.

The typical mean displacements in X-, Y- and Z-directions at each deformed state are plotted in Fig. 10. Notice that here the formula $D_z = \sqrt{\frac{w_1^2 + w_2^2 + \dots + w_n^2}{n}}$ is adopted to calculate the mean displacement in the Z-direction, which better reflects the contribution of the displacement at each pixel. Where, w_i is the w -displacement in i th pixel, and n is the number of pixels. This method is also adopted for the calculation of D_x , and D_y . The general trend is that D_z is always largest and followed by D_x , while the D_y is not obvious at the end of dynamic loading. An inspection of Fig. 10(a) indicates for $\theta = 0^\circ$, D_x increases gradually with dynamic loading to the peak stress after which it shows a downward trend at $V_i = 13$ m/s. The reason is that at this impact velocity, the specimen is not damaged, and the strain recovery phenomenon occurs after the peak value, as shown in Fig. 8(a) and Table 1. Accordingly, the stress-strain is categorised as Class I type. When V_i reaches 17 m/s, the specimen is

Table 2
Evolutions of out-of-plane displacement with loading time.

V_i (m/s)	θ (°)	Out-of-plane-displacement fields by 3D-DIC					AB profile
		t = 50 μ s	100 μ s	150 μ s	200 μ s	250 μ s	
13	0						
17							
17	60						
17	90						

completely damaged, and the deformation in the X direction keeps increasing after the peak value, as shown in Fig. 10(b). Here, the stress-strain response is Class II type. At this impact velocity, D_z slowly increases at the initial loading, and after the peak stress, the deformation dramatically accelerates indicates that macrocracks are generated within the specimen. The trend of deformation response at $\theta = 90^\circ$ is similar to that at $\theta = 0^\circ$, despite a reduced D_x and an amplified D_z at the end of loading (Fig. 10(d)). In addition, it is worth noting that for $\theta = 0^\circ$ and 90° , the D_x is much greater than D_z before peak stress, indicating that the deformation is mainly compression in the X direction, and the expansion in the Z direction is not apparent. After the peak stress, the deformation in the Z direction is accelerated, which ultimately results in D_z being greater than D_x . For $\theta = 60^\circ$, the deformation in X and Z directions is similar at the initial loading stage, while D_z is greater than D_x since 75μ s and after that the difference keeps growing as demonstrated in Fig. 10(c).

The mean deformation velocity V_x , V_y and V_z in the X-, Y- and Z-direction at each deformed state are extracted and shown in Fig. 11, which corresponds to Fig. 10. The total velocity V_{total} calculated by $\sqrt{V_x^2 + V_y^2 + V_z^2}$ is also plotted in Fig. 11. For $\theta = 0^\circ$ and 90° , V_z increases rapidly when coal specimen is approaching its peak stress, after which it is steadily raised up to the peak and then gradually reduces. The reduction of V_z results from the separation of fragments from the surface. Besides, V_x dominates at the initial loading stage, but as the stress is approaching the peak, the maximum rate of deformation is found in the Z direction. However, for $\theta = 60^\circ$, V_z always dominates during the whole loading process.

The maximum total velocity is defined as ejection velocity in this study, and the effect of impact velocities and bedding angles on the ejection velocity is provided in Fig. 12. The ejection velocity is positively correlated with the impact velocity since more energy is converted into kinetic energy in flying fragments with increasing impact velocities. Similar trends of coal ejection velocity with varying impact velocities

are found for cases with $\theta = 30^\circ$, 45° and 60° , among which, the highest and lowest the ejection velocities are identified in cases with $\theta = 45^\circ$ and $\theta = 60^\circ$, respectively. The ejection velocity ranges from 10.4 to 21.7 m/s for $\theta = 45^\circ$ with the given range of impact velocity, while it changes from 10.4 to 21.7 m/s for $\theta = 60^\circ$. The ejection velocity grows slowly from 4.34 m/s at $V_i = 10$ m/s, to 7.6 m/s at $V_i = 13$ m/s for $\theta = 0^\circ$, and then rapidly increases to 23 m/s when the V_i reaches 17 m/s. However, the increment of ejection velocity slows down with the further increase in strain rates, and finally, the ejection velocity is 28.1 m/s at $V_i = 21$ m/s. For $\theta = 90^\circ$, the coal ejection velocity rapidly increases from 3.4 m/s at $V_i = 10$ m/s to 21 m/s at $V_i = 13$ m/s, after which the increment of ejection velocity slows down with increasing impact velocities. The maximum ejection velocity is found at $\theta = 45^\circ$ from $V_i = 10$ –13 m/s, possibly because that 45° oriented specimens are more likely to slide along the beddings under this range of impact velocities. At $V_i > 13$ m/s, the maximum ejection velocity is always found at $\theta = 90^\circ$, indicating that coal specimens have a strong tendency for separating along the bedding direction at the high impact velocity.

3.4. Post-failure states

Table 3 presents typical post-failure states of coal specimens under coupled biaxial static and dynamic loading conditions. A clear strain-rate dependence of coal fragmentation can be observed for all bedding angles, i.e., the degree of fragment increases with increasing impact velocities. For $\theta = 0^\circ$ and $\theta = 90^\circ$, the applied dynamic loading is insufficient to break coal specimens at a low impact velocity, therefore specimens still keep partially intact. The common observation is splitting failure of exposed surfaces, and damage degree decreases from unconfined surface to the centre of the specimen. The similar phenomenon is observed in the quasi-static biaxial tests of layered rocks.^{35,89} However, coal specimens with splitting failure have not been completely damaged and still has a certain bearing capacity. The above failure modes of tensile splitting correspond to the Class-I stress-strain type

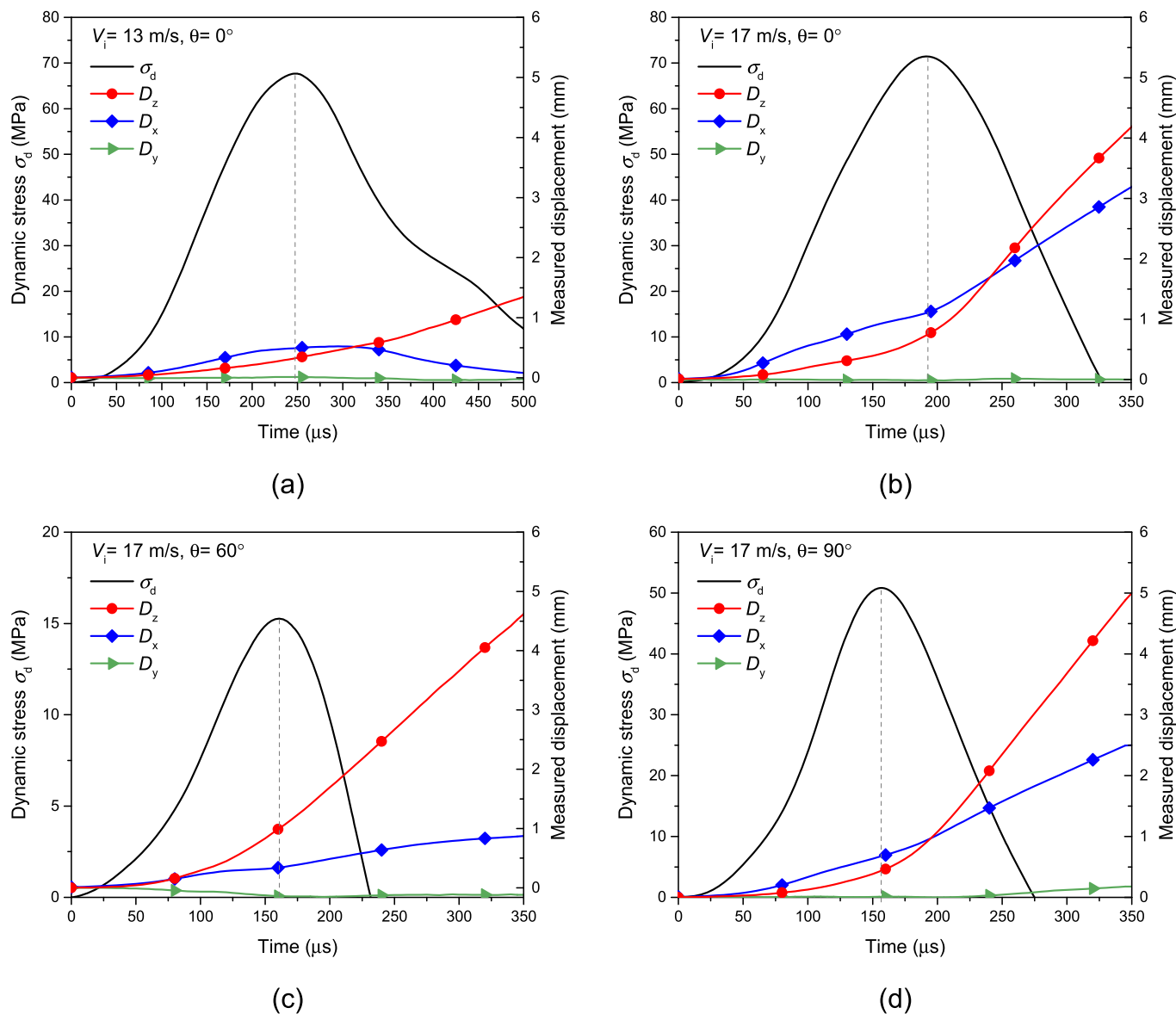


Fig. 10. Coal stress response and deformation with loading time at (a, b) different impact velocities and (b, c, d) bedding angles.

(Fig. 8(a) and (e) and Table 1), namely, the strain reduces gradually with the decrease of stress at the post-peak stage. Specimens are shattered into multiple fragments as the impact velocity further increases. Specimens with multiple fractures are characterised by some large fragments whose mean size is larger than 15 mm. Coal specimens are pulverised into hundreds of small fragments when the strain rate exceeds the critical value. Failure modes of multiple fracture and pulverization correspond to the Class II of stress-strain type. For $\theta = 30^\circ, 45^\circ$ and 60° , coal specimen has been shattered into multiple fractures at $V_i = 10$ m/s, and specimens are further fragmented to fine debris with increasing impact velocities. Correspondingly, stress-strain curves at these bedding orientations all belong to Class-II types as shown in Fig. 8(b)–(d). Besides, the fragmentation degree of coal specimen at these angles, especially at $\theta = 60^\circ$, is apparently high compared with $\theta = 0^\circ$ and $\theta = 90^\circ$ at the same impact velocity.

The internal fracture morphology of coal specimens is identified by X-ray CT at the Imaging and Medical beamline (IMBL) in the Australian Synchrotron. Compared with traditional laboratory-based micro-CT, synchrotron beamlines with high energy can penetrate deeper into the matter to acquire high spatial resolution with shorter scanning time. The detailed introduction of synchrotron X-ray CT can refer to.⁵³

Considering that even an impact velocity of 10 m/s can shatter specimens with $\theta = 30^\circ, 45^\circ$ and 60° into multiple fragments and make X-ray CT scanning impossible, specimens at these bedding angles were loaded at a relatively low impact velocity of around 7.5 m/s (strain rate ~ 50 s⁻¹) so that specimens can maintain good integrity for CT scanning. Table 4 summarises X-ray CT images before and after dynamic tests for different bedding angles at a low impact velocity. The selected 2D slice is along the X direction and is located in the centre of the Y-Z plane. The cracks, macerals and minerals are represented in dark grey, grey and white, respectively, as the increase of material density contributes to an increased X-ray opacity. 3D imaging is reconstructed from the collected data using Aviso 9.7 package combining with the capabilities of MASSIVE supercomputer cluster, which can offer abundant state-of-the-art image data processing and analysis features. Details of the image processing and segmentation procedures can be referred to Refs. 53,90. The results show that internal cracks are both caused by tensile stresses for coal specimen at $\theta = 0^\circ$ and 90° . When the impact direction is perpendicular to the bedding orientation ($\theta = 0^\circ$), cracks propagate along the impact direction, and they finally either change propagation direction or terminate in the maceral-mineral boundary as indicated as yellow arrows in Table 4. When the impact direction is

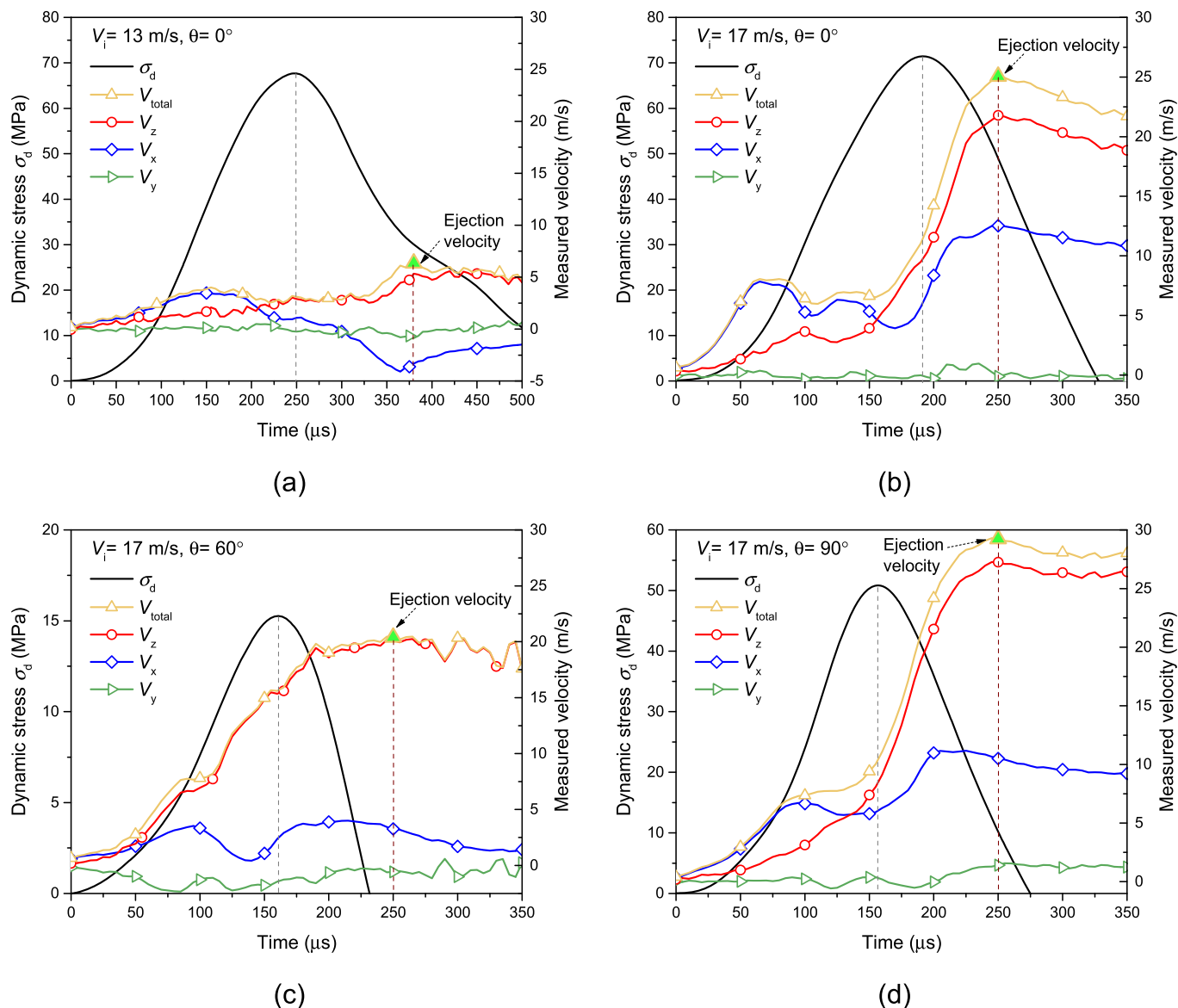


Fig. 11. Motion velocity of coal surface with loading time for different impact velocities (a, b) and bedding angles (b, c, d).

parallel to the bedding orientation ($\theta = 90^\circ$), newly formed cracks normally propagate along mineral-maceral boundaries. The newly generated cracks at mineral-maceral interfaces are probably attributed to stress concentrations and localised weaknesses at grain-grain boundaries.⁹¹ Furthermore, much more cracks are observed at $\theta = 90^\circ$ compared with that at $\theta = 0^\circ$ at the similar impact velocity. The bearing capacity of coal specimens is not significantly enhanced even though at high impact velocities since the occurrence of extensive cracks weakens the effect of strain rate for $\theta = 90^\circ$. By contrast, more energy needs to be consumed for cracks to cross the mineral phase at $\theta = 0^\circ$ than to propagate along the mineral-maceral boundary at $\theta = 90^\circ$. Therefore, more energy is absorbed to break coal specimens thoroughly at $\theta = 0^\circ$, which correspondingly enhances peak stresses. For coal specimens with $\theta = 45^\circ$ and 60° , the generated cracks are mainly shear ones propagating along with the bedding layers, which has a controlling effect on the specimen failure. The cracks that cross the bedding plane are also observed, which are connected with the cracks on the bedding planes to form a V-shaped crack band. For the specimen with $\theta = 30^\circ$, the newly cracks are mainly tensile ones that propagate along the impact direction, although a few shear cracks exist along the bedding planes. Overall, as the θ increases, the contribution of bedding planes to the failure of coal specimens

becomes small.

3.5. Fragment size distribution

After each test, coal fragments were carefully collected to perform sieve tests in order to quantitatively and intuitively analyse fragmentation characteristics in coal bursts.⁸⁶ Standard sieves with mesh diameters of 1.18, 2, 2.8, 3.35, 6.4, 9.5, 11.2, and 19 mm are adopted. Fig. 13 shows typical fragment size distributions of post-failure coal specimen at the impact velocity (V_i) of 13 and 21 m/s at $\theta = 0^\circ$. At $V_i = 13$ m/s, coal fragments with a size larger than 19 mm are in the majority of the mass weight, while a large amount of debris with a size smaller than 6.4 mm is observed at $V_i = 21$ m/s. Fig. 14 presents the cumulative mass fraction of fragments passing through a certain sieve size as a function of impact velocities and anisotropic angles. Increasing impact velocities contributes to a large proportion of fine fragment sizes, as indicated by the steep slope of the fragment size distribution in Fig. 14 (a). Moreover, the fragment-size composition is also dependent on the bedding angles, as shown in Fig. 14(b). At $V_i = 17$ m/s, coal specimens with bedding angle $\theta = 60^\circ$ have the finest fragmentation where 63.2% of fragments whose size is less than 5 mm, while the smallest

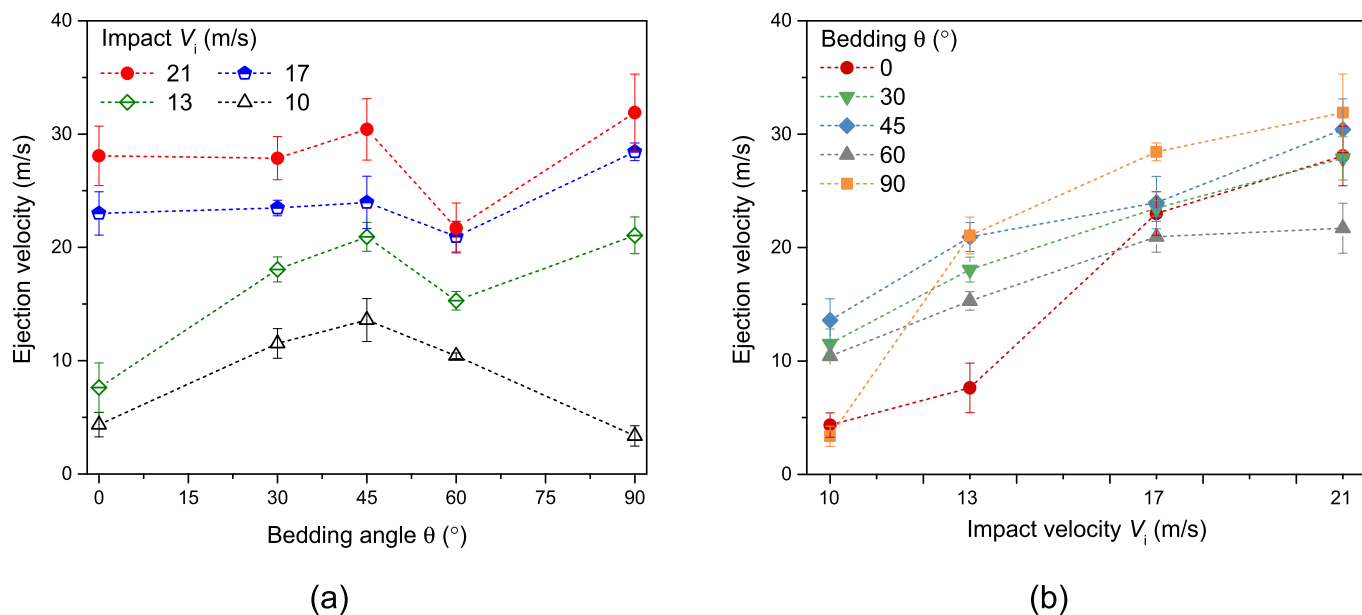


Fig. 12. Variation in coal ejection velocity as a function of (a) anisotropic angles and (b) impact velocities.

Table 3
Post-failure states of coal specimen after coupled biaxial static and dynamic tests.

$\theta(^{\circ})$	0	30	45	60	90
10					
13					
17					
21					

fragmentation is found at $\theta = 90^{\circ}$ where fragments with the size smaller than 5 mm account for 44.5%. Although the cumulative percentage of fragment sizes less than 5 mm is rapidly increasing, the decelerated growth trend is observed when the size is greater than 5 mm, especially for $\theta = 0^{\circ}$.

Fig. 15 summarised fragment size evolutions characterised by mean values and standard deviations for five bedding angles at various impact

velocities. Here, the average size of coal fragments is analysed by.⁹²

$$d_m = \frac{\sum(\gamma_i \cdot r_i)}{\sum \gamma_i} \tag{14}$$

where r_i is the mean size of the fragments situated between sieves and successive mesh size and γ_i is the mass fraction of fragments corresponding to the size r_i .

Table 4
2D slice and 3D reconstruction of X-ray CT images before and after tests at a low impact velocity for different bedding angles.

θ ($^{\circ}$)	V_i (m/s)	$\dot{\epsilon}$ (s^{-1})	States	2D slice	3D reconstruction		
					Cola matrix	Mineral phase	Fracture network
0	10.6	86.3	Pre-impact				
			Post-impact				
30	7.8	53.6	Pre-impact				
			Post-impact				
45	7.2	49.1	Pre-impact				
			Post-impact				

(continued on next page)

Table 4 (continued)

θ (°)	V_i (m/s)	$\dot{\epsilon}$ (s ⁻¹)	States	2D slice	3D reconstruction		
					Cola matrix	Mineral phase	Fracture network
60	7.7	52.2	Pre-impact				
			Post-impact				
90	9.7	77.2	Pre-impact				
			Post-impact				

* θ , V_i and $\dot{\epsilon}$ mean bedding angle, impact velocity and strain rate, respectively.

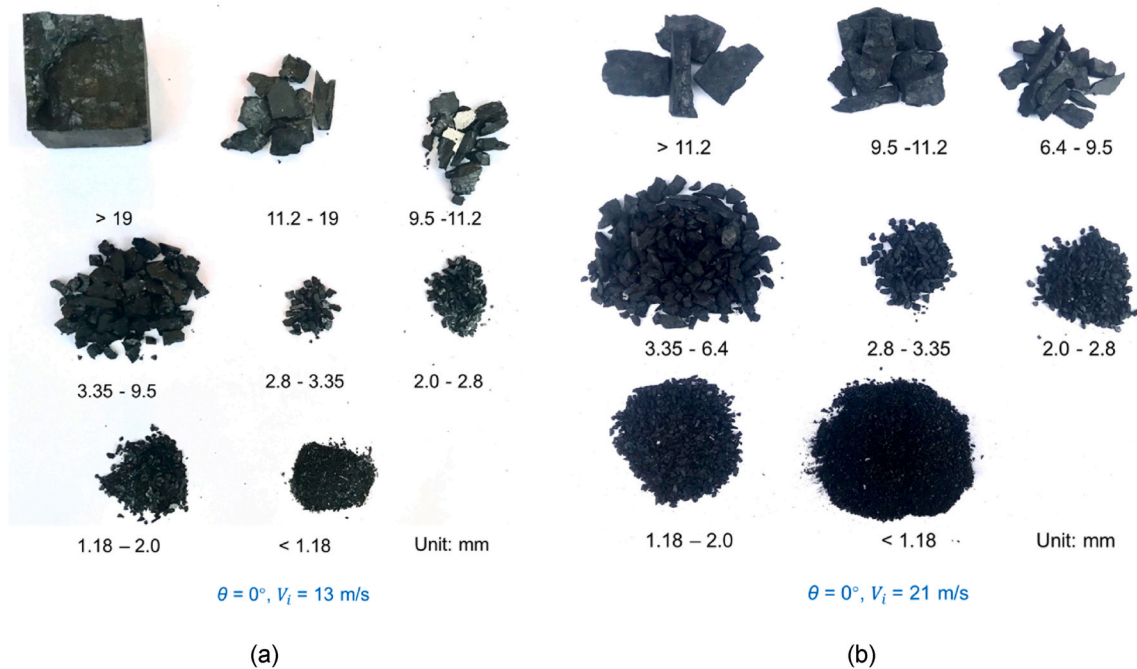


Fig. 13. Typical coal fragment size distribution of coal specimen at $\theta = 0^\circ$ under impact velocities of (a) 13 m/s and (b) 21 m/s.

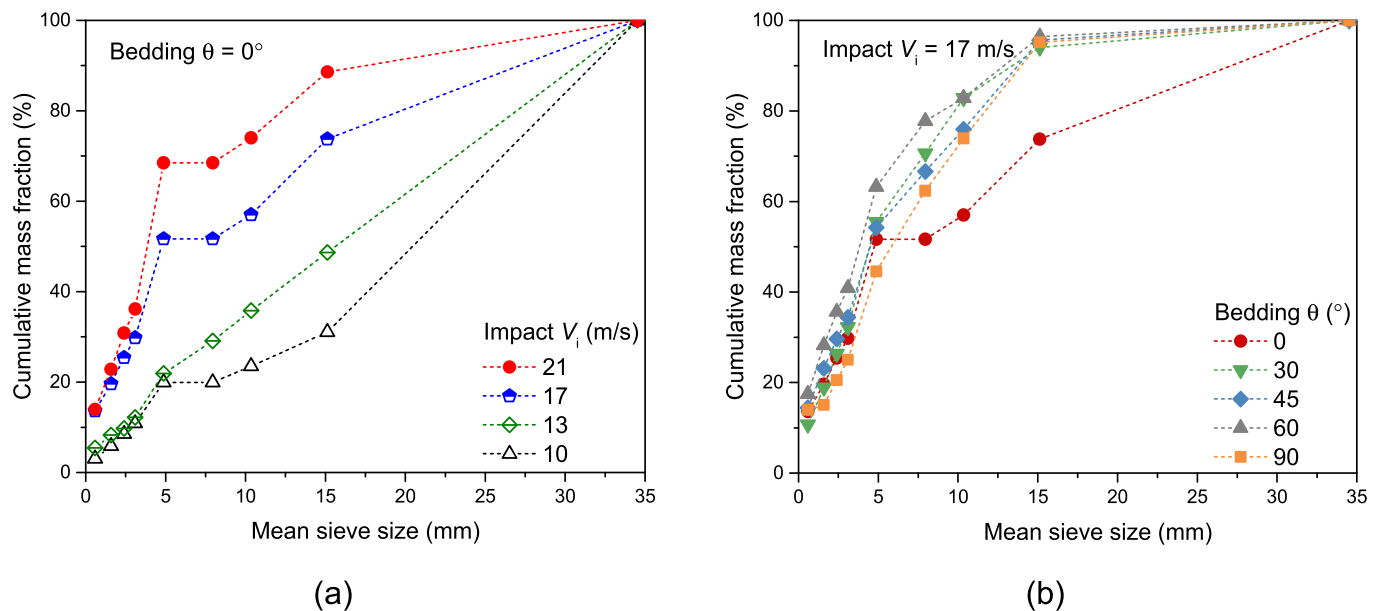


Fig. 14. Variation in fragment size distribution as a function of (a) impact velocities and (b) anisotropic angles.

For all bedding angles, coal fragment size exhibits a decreasing trend with the increase of impact velocities, and the decreasing degree is significant when $V_i < 17$ m/s, as shown in Fig. 15(a). The significant decrease of mean fragment size is observed at $\theta = 0^\circ$ from 37.6 to 7.5 mm (by 80.3%) when V_i is from 13 to 21 m/s. On the contrary, the coal fragmentation at $\theta = 60^\circ$ shows the least sensitivity to the impact velocity manifested as fragment size ranging from 16.9 to 5.8 mm. Apart from that, coal specimens with bedding angle $\theta = 60^\circ$ always show the smallest fragment size at specific impact velocity, as indicated in Fig. 15 (b). For example, the mean fragment size at $\theta = 60^\circ$ is 9.9 mm, while this value is 29.8 mm for $\theta = 0^\circ$ at $V_i = 13$ m/s. The negative correlation between fragment size distribution and dynamic peak stress can be observed when comparing Figs. 15 and 9. It can be explained that

increasing strain rates enhance the bearing capacities, but at the same time, it leads to increasing activated microcracks and subsequently increases the number of broken fragments.

3.6. Effect of energy absorption on ejection velocity and fragmentation

The dynamic incident, reflected, transmitted and absorbed energy of coal specimen under biaxial pre-stress conditions can be obtained based on Eqs. 6–12. Fig. 16 demonstrates histories of energy evolutions for coal specimens with bedding angles of $\theta = 0^\circ, 30^\circ, 45^\circ, 60^\circ$ and 90° at $V_i = 17$ m/s. It can be seen that at different bedding angles, the evolution of various energies is similar in the deformation and fracturing stages. The incident energy and reflection energy increase slowly at the initial

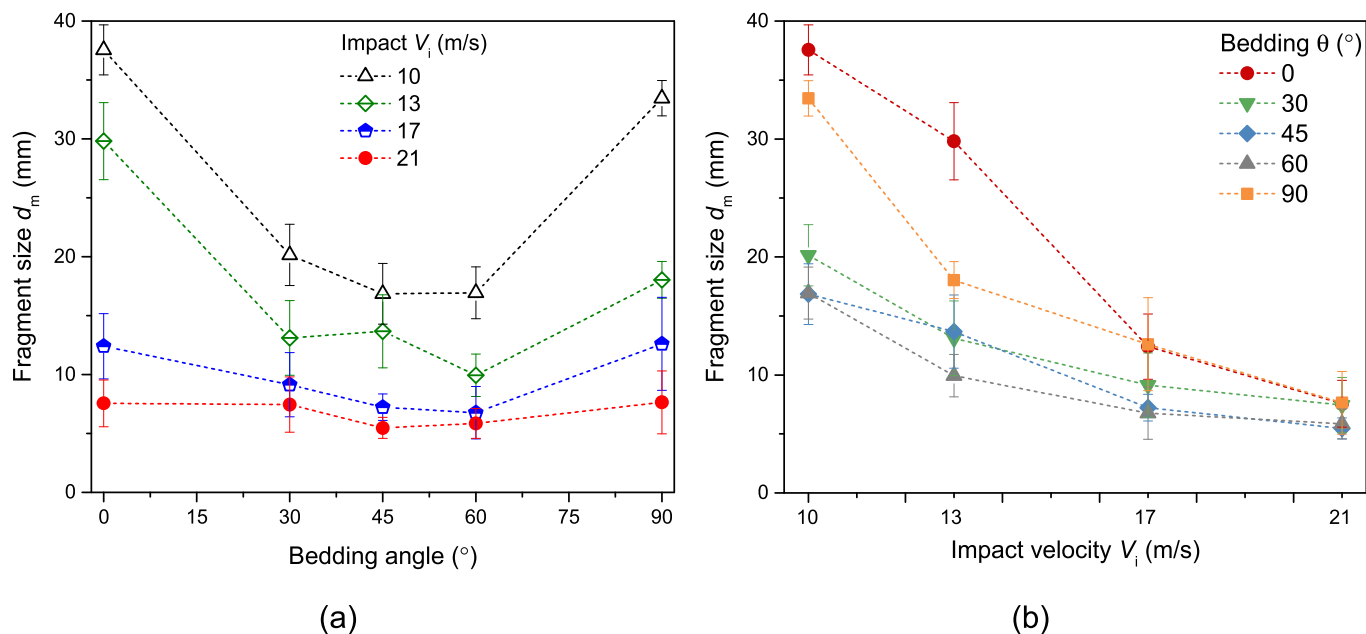


Fig. 15. Variation in mean fragment size as a function of (a) anisotropic angles and (b) impact velocities.

dynamic loading stage, while since around $100 \mu\text{s}$ these energies increase sharply until the energy remains constant after a certain value. The reflected energy has a significant difference at different bedding angles due to their impedance variances between the incident bar and coal specimens. The largest reflection energy is observed at $\theta = 60^\circ$ while the lowest value is found at $\theta = 0^\circ$. The energy absorption abilities also vary resulting from the bedding effect. Since a large amount of input energy is reflected, only a small part of the energy is consumed for the specimens at $\theta = 60^\circ$. Besides, the transmission energy keeps low value and varies slightly for $\theta = 30^\circ, 45^\circ$ and 60° indicating that most input energies are consumed to fracture specimens.

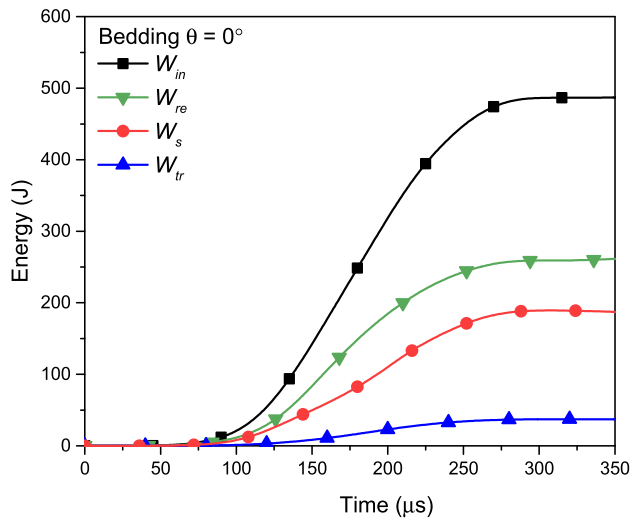
Fig. 17(a) summarised the relationships of the absorption energy with incident energy at different bedding angles, where the energy absorption W_s is derived from Eq. (6). A general trend is that the absorption energy increases with increasing incident energy. The absorption capacity of coal specimens at $\theta = 0^\circ$ has a slight upward trend when the input energy is less than 300 J ($V_i = 13 \text{ m/s}$), after that it increases quickly and stably. The reason for the transition phenomenon is probably attributed to the changes in coal failure modes.⁹² Coal specimens show split failure at $\theta = 0^\circ$ when $V_i < 13 \text{ m/s}$, and above the critical impact velocity, they are fractured into pulverised small fragments as shown in Table 3. Therefore, 300 J of incident energy is transition energy from split to fracture for coal specimens with bedding angle $\theta = 0^\circ$. The transition phenomenon is also observed for coal specimens with bedding angle $\theta = 90^\circ$. However, no energy transitions are found for $\theta = 30^\circ, 45^\circ$, and 60° , and the energy at these bedding angles gradually increases with more energy input. A close observation of failure modes in Table 3 indicates that coal specimens with these bedding orientations have been fractured at $V_i = 10 \text{ m/s}$. Fig. 17(b) demonstrates that the trend of ejection velocity with increasing absorbed energy. For all bedding angles, ejection velocity sees an increase with improving absorbed energy, but the growth rate shows a downward trend. With the same energy absorption, the highest ejection velocity is found at $\theta = 45^\circ$, while to achieve the same ejection velocity, the 0° oriented coal specimens require the highest absorbed energy. The relationship between the ejection velocity of coal fragments with peak stresses is also demonstrated in Fig. 17(c). A positive correlation between them can be found due to they both enhance with increasing strain rates. Obviously, the 90° oriented specimen is the most sensitive to variation of peak stress: the peak stress only increase from 40.55 MPa to 48.62 MPa (by 19.9%), but

ejection velocity increases sharply from 3.36 m/s to 32 m/s with an increase of over 8.5 times. Fig. 17(d) presents the relationship between the average fragment size and energy absorption at different bedding angles. The trends are somewhat similar for all bedding angles: the fragment size keeps decreasing as absorption energy increases. For the same fragment size, the energy consumption for $\theta = 0^\circ$ is greater than that in other angles. In other words, to achieve the same fragment degree, coal specimens at $\theta = 0^\circ$ consume maximum energy. On the contrary, the minimum energy consumption required to achieve the same damage degree is found for $\theta = 60^\circ$.

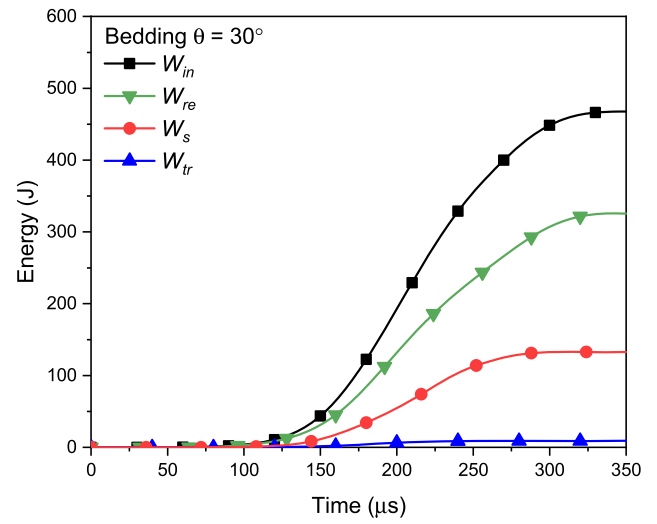
4. Discussion

The coal burst is one of the most serious and least understood problems in mining operations all around the world. Although great efforts have been made to explain its phenomenon, there is still huge potential for further research. In this work, coal bursts were reproduced under experimental conditions to understand the influence of the strain rate $\dot{\epsilon}$ and bedding angle θ on coal dynamic failures. Our experimental results show that for coal specimens with any bedding angles, increasing impact velocity (or $\dot{\epsilon}$) leads to an increase of peak stresses (Fig. 9(b,c)) and absorbed energy (Fig. 17(a,b)), but on the other hand, the speed of the flying fragments also increases (Fig. 12(b)). Besides, the bedding angles have an obvious dominated effect on coal fragment size and ejection velocity at a low $\dot{\epsilon}$, while as the $\dot{\epsilon}$ increases, its effect gradually becomes weak. In engineering applications, it is particularly important to determine the magnitude and direction of dynamic loads for safety support for a specific coal seam structure. For example, when the orientation of dynamic loads and the coal seam is around 45° , the support strength should be increased, or a strong energy-absorbing support system should be adopted to prevent potential hazards.

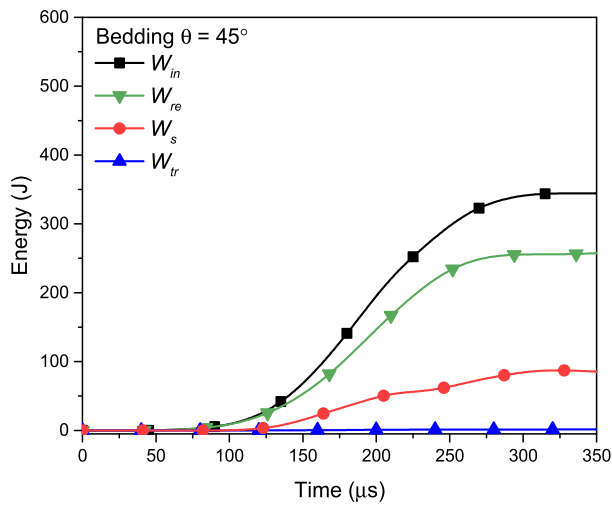
Energy evolution analysis plays an important role in investigating the mechanism of coal burst disasters. The amount of energy absorbed by the coal mass directly determines the coal burst severity since it controls the speed of flying fragments.^{18,93} Our work shows that as the absorbed energy W_s increases, the ejection velocity v_e of coal fragments gradually increases, but the growth rate exhibits a downward trend (Fig. 17(b)). W_s can be divided into three parts: kinetic energy W_k , dissipated energy W_f and other forms of energy W_o (e.g., thermal energy). W_k is associated with flying fragments while W_f is used to create



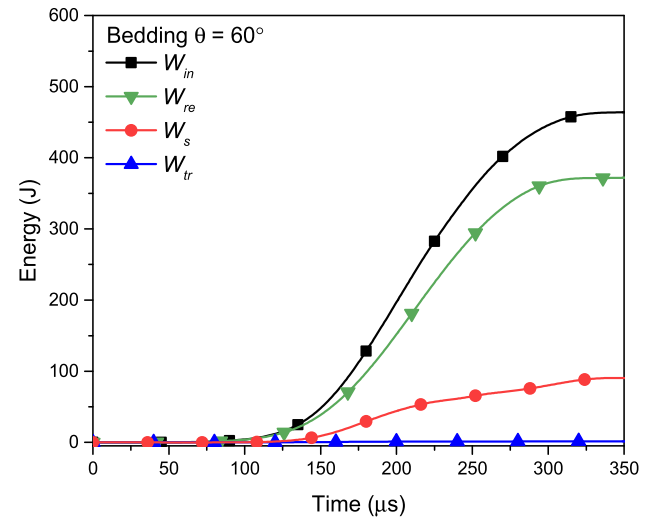
(a)



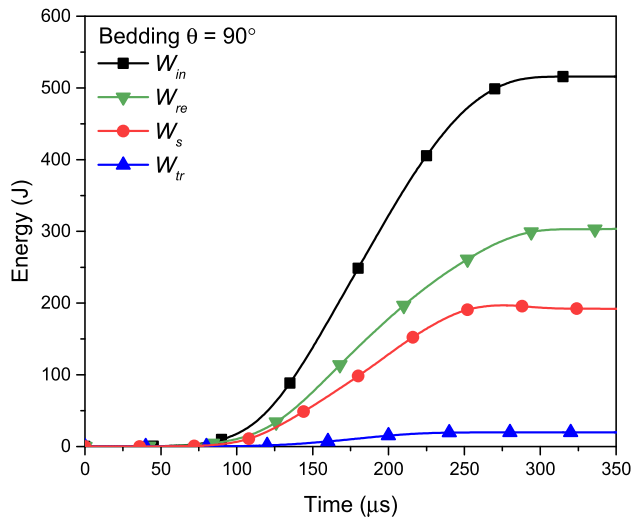
(b)



(c)



(d)



(e)

Fig. 16. Typical energy evolutions for different bedding angles at the impact velocity of 17 m/s.

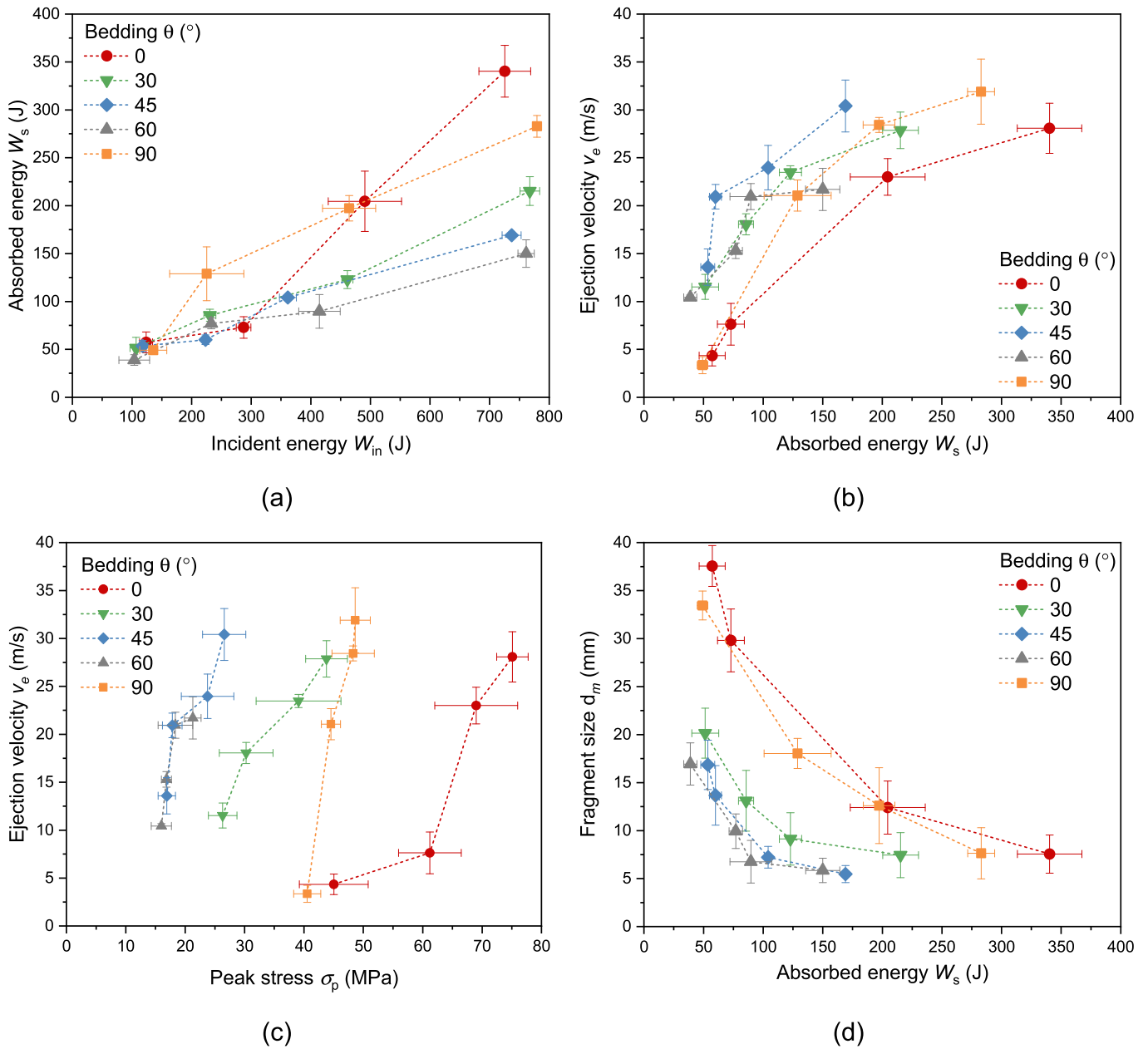


Fig. 17. The change of absorbed energy with incident energy (a), the variation in ejection velocity (b) and fragment size (d) with absorbed energy, and the relationship between ejection velocity and peak stress (c).

fracture surface and micro-cracks.^{94,95} The W_0 is assumed to be very small and negligible in this study since the strain rate is not very high, thus $W_s = W_k + W_f$. Assume that the mass and velocity of flying fragments are m_e and v_e , respectively, as shown in Fig. 18, the relationship between v_e and W_k can be expressed as $W_k = \xi W_s = \frac{1}{2} m_e v_e^2 = \frac{1}{2} \lambda m_0 v_e^2$,

therefore, $v_e = a\sqrt{W_s}$, where $a = \sqrt{\frac{2\xi}{\lambda m_0}}$, m_0 is the mass of tested coal specimen, $\xi = W_k/W_s$ and $\lambda = m_e/m_0$. If ξ and λ keep unchanged at different $\dot{\epsilon}$, the coefficient a remains the same, and $v_e \propto \sqrt{W_s}$. However, the fact is that increasing $\dot{\epsilon}$ will cause a variation of ξ and λ . Normally,

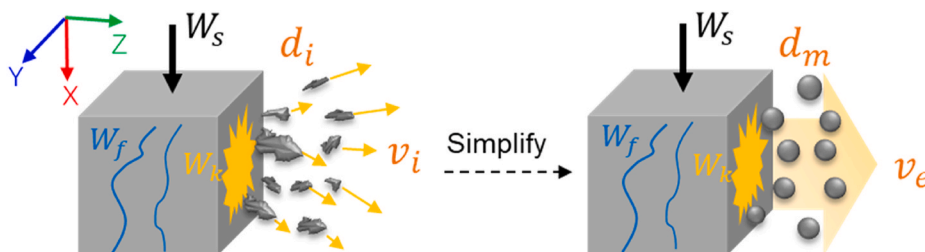


Fig. 18. Energy distribution in coal burst process. W_s , W_f , and W_k mean absorbed energy, dissipation energy and kinetic energy, respectively.

the parameter λ grows with the increase of $\dot{\epsilon}$ since more fragments fly out at a higher $\dot{\epsilon}$. According to our experimental observation, λ approximately ranges from 10% to 30% at the strain rate of 80–250 s⁻¹. The parameter ξ also shows increasing trends with increasing $\dot{\epsilon}$ and its value ranges from 4% to 7% based on previous research in dynamic tensile tests.⁹⁵ Therefore, a is probably fluctuant with increasing $\dot{\epsilon}$. Our experimental data indicate a mainly ranges from 1 to 3 (Fig. 19(a)), however, the specific values of ξ and λ for coal under the influence of $\dot{\epsilon}$ need further research, such as utilising numerical simulation, which is also our next research work. Besides, sufficient attention should be paid to the effect of bedding angles on v_e . Under the same energy absorption, the highest v_e is found at $\theta = 45^\circ$ while the lowest is at $\theta = 0^\circ$, which is attributed to different values of ξ and λ . According to the above analysis, the following two strategies can be adopted to reduce coal burst hazards in mining operations: reducing the absorption energy of coal mass or input energy from dynamic loads; and avoiding/preventing dynamic loads induced on the angle of 45° to the bedding planes.

Coal fragmentation is also closely related to W_s : the coal fragment size gradually decreases as W_s increases but the decline rate tends to be slow as demonstrated in Fig. 17(d). Assume that coal fragments are spherical with an average size d_m , as shown in Fig. 18, the dissipated energy W_f can be estimated by^{18,93,96,97}: $W_f = (1 - \xi)W_s = G_f A_f = G_f \left(\frac{6V_0}{d_m} - A_0 \right)$, where G_f is surface energy, which is defined as the energy required to create one unit of surface area^{53,98,99}; A_f means newly created crack surface area; V_0 and A_0 are the volume and area of the coal specimen before the test, respectively. Therefore, the relationship between d_m and W_s can be written as: $\frac{1}{d_m} = bW_s + \frac{1}{d_0}$, where $b = \frac{1-\xi}{6V_0G_f}$, and d_0 is the length of initial cubic specimens. Apparently, d_m is negatively W_s -dependent if the effect of $\dot{\epsilon}$ is ignored. However, G_f generally enhances with increasing $\dot{\epsilon}$ ^{100,101} and meanwhile considering that a negative correlation between $(1-\xi)$ and $\dot{\epsilon}$, thus parameter b should decrease monotonously with growing $\dot{\epsilon}$. Currently, the parameter b , in theory, has yet to be further determined, but for our experimental data, b mainly ranges from 0.2 to 1.2, as shown in Fig. 19(b). Besides, it is worth noting that θ has a great effect on b : b tends to be low at $\theta = 0^\circ$ and $\theta = 90^\circ$ compared with that at other bedding angles, which is caused by the different values of G_f and ξ .

The anisotropic failure behaviours caused by bedding structures in peak stress, ejection velocity and fragmentation are attributed to the

different failure modes. In this work, for the first time, we revealed the effect of bedding angles on crack types and the crack propagation process of biaxially confined coal under dynamic loading by X-ray CT scanning (Table 4). Acoustic emission (AE) and/or microseismic monitoring, as another promising non-destructive detection technology, has been widely used in the laboratory and real mining environment,^{102–107} and the damage process of tested materials can be observed during the entire load history.¹⁰⁴ However, until now, monitoring and analysis of AE signals under dynamic loads are still substantially challenging due to the extremely short loading time and complex stress waves propagated in the tested specimen. Capturing reliable and unsaturated raw signals, and separating AEs radiated by cracks from raw signals are keys to solving these problems.

5. Conclusions

The mechanical and fracturing properties of coal with inherent bedding planes under the coupled biaxial static-dynamic loading conditions were examined using a Triaxial Hopkinson bar system in combination with the high-speed 3D-DIC technique and synchrotron-based X-ray CT. The coupling effect of bedding planes and strain rates on stress-strain response, ejection process and fragmentation characteristics of coal bursts were analysed in detail. The following main conclusions are summarised as:

Under the same biaxial confinement, the peak stresses enhance with increasing impact velocities, while its growth rate constantly decreases. An index R_c is used to describe coal anisotropic behaviour in strength. The results indicate that coal strength anisotropy is mainly affected by bedding structures at $V_i < 17$ m/s then dominated by strain rates at $V_i \geq 17$ m/s. In a coal burst, the coal ejection velocity is positively correlated with impact velocities. However, growing impact velocities tend to weaken the difference in the ejection velocity of coal specimens with different bedding orientations. As the loading level increases, the coal fragmentation shows an increasing tendency, with failure modes changing from tensile splitting, multiple fracture to pulverization. Specifically, the obvious downward trend of fragment size with rising strain rates is found at $\theta = 0^\circ$ and 90° .

The peak stresses exhibit a “U” shape against bedding orientations at a given impact velocity, and the highest and lowest values are found at $\theta = 0^\circ$ and 60° , respectively. The strain rate sensitivity of peak stress varies with anisotropic angles. Coal specimens with bedding

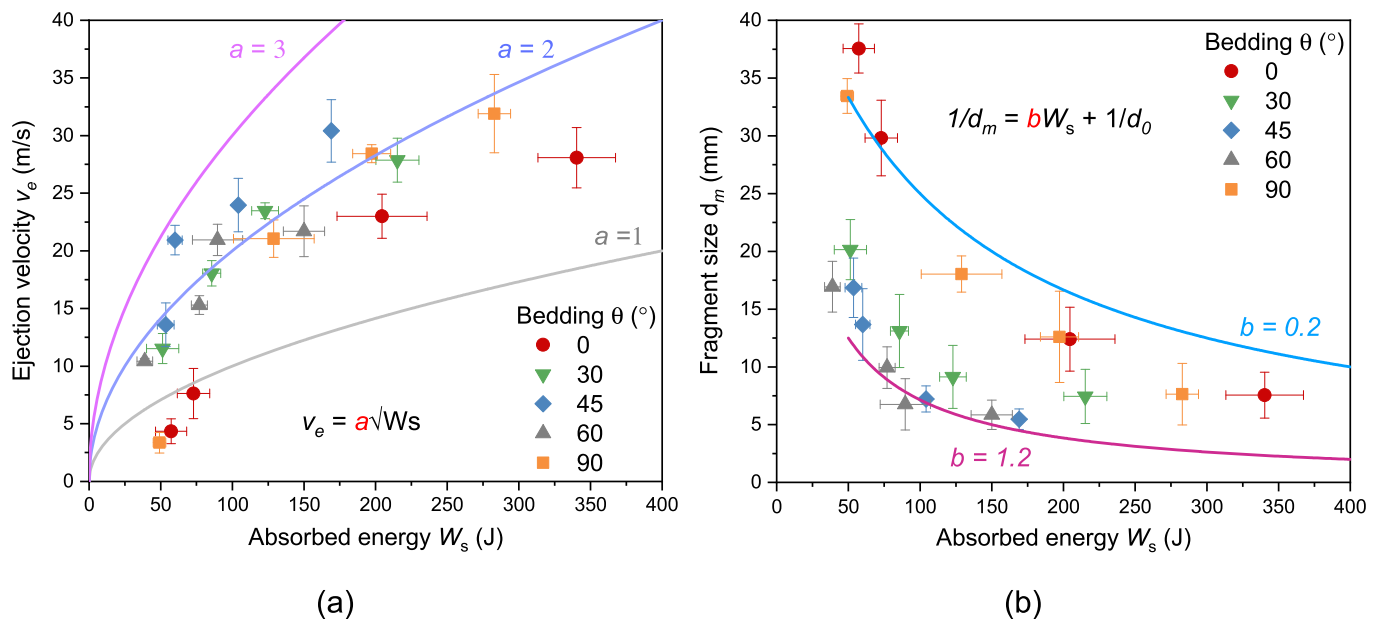


Fig. 19. The trend of ejection velocity (a) and fragment size (b) with increasing absorbed energy.

orientations in the range of 0° – 45° are more sensitive to strain rates, while specimens oriented from 60° to 90° have low rate sensitivity. The bedding plane also heavily affects ejection velocity in a coal burst. The maximum coal ejection velocity is found at $\theta = 45^\circ$ when $V_i < 13$ m/s ($\dot{\epsilon} < 130$ s $^{-1}$), and then it remains at $\theta = 90^\circ$ when $V_i > 13$ m/s. The distribution of coal fragment size is affected by the bedding orientation while its effect declines with growing strain rates, especially when $V_i > 17$ m/s ($\dot{\epsilon} \geq 190$ s $^{-1}$). The maximum fragment size of coal specimens is observed at $\theta = 0^\circ$, while the minimum one is found at $\theta = 45^\circ$ or 60° at the same impact velocity. Moreover, to achieve the same fragment degree, the maximum energy needs to be absorbed for coal specimens with bedding angle $\theta = 0^\circ$, but the minimum energy needs to be consumed for $\theta = 60^\circ$.

The testing using the Triaxial Hopkinson bar system is valuable in its capability of replicating coal bursts under the effect of complex *in-situ* geological conditions and unique physical properties of coal specimens. Experimental results indicate that coal bursting behaviours under coupled biaxial static and dynamic loading conditions are dependent on bedding angles and strain rates. However, there seems to be a competitive relationship between these two factors. The bedding plane is the major controlling factor for mechanical and fracturing properties of coal specimens, but increasing strain rates gradually weaken the bedding effect.

Declaration of competing interest

The authors declare that they have no known competing financial interests or personal relationships that could have appeared to influence the work reported in this paper.

Acknowledgement

This work was financially supported by the Australian Research Council (LE150100058 and DE200101293). The first author would like to acknowledge the financial support from the China Scholarship Council-Monash University Postgraduate Scholarship (201706420060). The specimens were scanned in the Imaging and Medical beamline (IMBL) at Australian Synchrotron (Project M13469). The coal surface morphologies were scanned at Monash Centre for Electron Microscopy. We also wish to thank Mr Lie Kong of Monash University, Australia, and Dr Zhigang Liu of Shandong University of Science and Technology, China, for fruitful discussions.

References

- Kaiser PK, McCreath DR, Tannant DD. *Canadian Rockburst Support Handbook*. Sudbury, Ontario: Geomechanics Research Centre; 1996:314.
- Kaiser PK, Cai M. Design of rock support system under rockburst condition. *J Rock Mech Geotech Eng*. 2012;4(3):215–227.
- Ortlepp WD, Stacey TR. Rockburst mechanisms in tunnels and shafts. *Tunn Undergr Space Technol*. 1994;9(1):59–65.
- Cai M. Principles of rock support in burst-prone ground. *Tunn Undergr Space Technol*. 2013;36:46–56.
- Feng GL, Feng XT, Chen BR, Xiao YX, Yu Y. A microseismic method for dynamic warning of rockburst development processes in tunnels. *Rock Mech Rock Eng*. 2014; 48(5):2061–2076.
- Bräuner G. *Rockbursts in Coal Mines and Their Prevention*. Rotterdam, Netherlands: Balkema; 1994.
- Iannacchione AT, Zelanko JC. Occurrence and remediation of coal mine bumps: a historical review. In: *Proceedings in Mechanics and Mitigation of Violent Failure in Coal and Hard-Rock Mines*. USBM Special Publication; 1995:27–67, 01–95.
- Ge M. Efficient mine microseismic monitoring. *Int J Coal Geol*. 2005;64(1–2):44–56.
- Wang GF, Gong SY, Dou LM, Li G, Cai W, Fan CJ. A novel experimental technique to simulate shock behaviour and bursting failure of roadways. *Shock Vib*. 2019;2019: 1–13.
- Tang CA, Wang J, Zhang J. Preliminary engineering application of microseismic monitoring technique to rockburst prediction in tunneling of Jinping II project. *J Rock Mech Geotech Eng*. 2010;2(3):193–208.
- Zhu S, Feng Y, Jiang F. Determination of abutment pressure in coal mines with extremely thick alluvium stratum: a typical kind of rockburst mines in China. *Rock Mech Rock Eng*. 2015;49(5):1943–1952.
- Wang GF, Gong SY, Dou LM, Cai W, Yuan XY, Fan CJ. Rockburst mechanism and control in coal seam with both syncline and hard strata. *Saf Sci*. 2019;115:320–328.
- Jiang Q, Su GS, Feng XT, Cui J, Pan PZ, Jiang JQ. Observation of rock fragment ejection in post-failure response. *Int J Rock Mech Min Sci*. 2015;74:30–37.
- Ortlepp WD. High ground displacement velocities associated with rockburst damage. *3rd Int Symp Rockbursts Seismicity Mines*. 1993:101–106.
- Stacey TR, Ortlepp WD, Kirsten HAD. Energy-absorbing capacity of reinforced shotcrete, with reference to the containment of rockburst damage. *J S Afr Inst Min Metall*. 1995;95(3):137–140.
- Milev AM, Spottiswoode SM, Rorke AJ, Finnie GJ. Seismic monitoring of a simulated rockburst on a wall of an underground tunnel. *J S Afr Inst Min Metall*. 2001;101(5):253–260.
- Diederichs MS. Early assessment of dynamic rupture hazard for rockburst risk management in deep tunnel projects. *J S Afr Inst Min Metall*. 2018;118(3):193–204.
- Yang XH, Ren T, Tan LH. Estimation of average ejection velocity generated by rock burst under compression load. *Int J Rock Mech Min Sci*. 2020:128.
- Frith R, Reed G, Jones A. A causation mechanism for coal bursts during roadway development based on the major horizontal stress in coal: very specific structural geology causing a localised loss of effective coal confinement and Newton's second law. *Int J Mining Sci Technol*. 2020;30(1):39–47.
- Shepherd J, Rixon LK, Griffiths L. Outbursts and geological structures in coal mines: a review. *Int J Rock Mech Min Sci Geomech Abstr*. 1981;18(4):267–283.
- Dou LM, Lu CP, Mu ZL, Gao MS. Prevention and forecasting of rock burst hazards in coal mines. *Min Sci Technol*. 2009;19(5):585–591.
- Islam MR, Shinjo R. Mining-induced fault reactivation associated with the main conveyor belt roadway and safety of the Barapukuria Coal Mine in Bangladesh: constraints from BEM simulations. *Int J Coal Geol*. 2009;79(4):115–130.
- Zhang CG, Canbulut I, Hebblewhite B, Ward CR. Assessing coal burst phenomena in mining and insights into directions for future research. *Int J Coal Geol*. 2017;179: 28–44.
- Iannacchione AT, Tadolini SC. *Coal Mine Burst Prevention Controls. Conference on Ground Control in Mining*. 2008.
- Li ZL, Dou LM, Cai W, et al. Investigation and analysis of the rock burst mechanism induced within fault-pillars. *Int J Rock Mech Min Sci*. 2014;70:192–200.
- Mark C. Coal bursts in the deep longwall mines of the United States. *Int J Coal Sci Technol*. 2016;3(1):1–9.
- He J, Dou LM, Cao AY, Gong SY, Lv JW. Rock burst induced by roof breakage and its prevention. *J Cent S Univ*. 2012;19(4):1086–1091.
- Mottahedi A, Ataei M. Fuzzy fault tree analysis for coal burst occurrence probability in underground coal mining. *Tunn Undergr Space Technol*. 2019;83:165–174.
- Cook N. The basic mechanics of rockbursts. *J S Afr Inst Min Metall*. 1963;64(3): 71–81.
- Hustrulid WA. A review of coal pillar strength formula. *Rock Mech*. 1976;8: 115–145.
- Vardoulakis I. Rock bursting as a surface instability phenomenon. *Int J Rock Mech Min Sci Geomech Abstr*. 1984;21(3):137–144.
- Kidybiński A. Bursting liability indices of coal. *Int J Rock Mech Min Sci Geomech Abstr*. 1981;18(4):295–304.
- Gong FQ, Yan JY, Li XB, Luo S. A peak-strength strain energy storage index for rock burst proneness of rock materials. *Int J Rock Mech Min Sci*. 2019;117:76–89.
- Tang SC, Liu XJ, Chen K. Study on the ejective debris of granite biaxial rockburst test. *Proc 5th Int Confer Mach Mater Comput Technol (ICMMCT 2017)*. 2017;126: 200–205.
- Zhang HW, Wan ZJ, Ma D, Zhang Y, Cheng JY, Zhang Q. Experimental investigation on the strength and failure behavior of coal and synthetic materials under plane-strain biaxial compression. *Energies*. 2017;10(4).
- Tarasov B, Potvin Y. Universal criteria for rock brittleness estimation under triaxial compression. *Int J Rock Mech Min Sci*. 2013;59:57–69.
- Wang JA, Park HD. Comprehensive prediction of rockburst based on analysis of strain energy in rocks. *Tunn Undergr Space Technol*. 2001;16:49–57.
- He MC, Miao JL, Feng JL. Rock burst process of limestone and its acoustic emission characteristics under true-triaxial unloading conditions. *Int J Rock Mech Min Sci*. 2010;47(2):286–298.
- Zhao F, He MC. Size effects on granite behavior under unloading rockburst test. *Bull Eng Geol Environ*. 2016;76(3):1183–1197.
- Li XB, Du K, Li DY. True triaxial strength and failure modes of cubic rock specimens with unloading the minor principal stress. *Rock Mech Rock Eng*. 2015;48(6): 2185–2196.
- Zhai SB, Su GS, Yin SD, Zhao B, Yan LB. Rockburst characteristics of several hard brittle rocks: a true triaxial experimental study. *J Rock Mech Geotech Eng*. 2020;12 (2):279–296.
- He MC, Nie W, Zhao ZY, Guo W. Experimental investigation of bedding plane orientation on the rockburst behavior of sandstone. *Rock Mech Rock Eng*. 2012;45 (3):311–326.
- Su GS, Feng XT, Wang JH, Jiang JQ, Hu LH. Experimental study of remotely triggered rockburst induced by a tunnel axial dynamic disturbance under true-triaxial conditions. *Rock Mech Rock Eng*. 2017;50(8):2207–2226.
- He M, Xia HH, Jia XN, Gong WL, Zhao F, Liang KY. Studies on classification, criteria and control of rockbursts. *J Rock Mech Geotech Eng*. 2012;4(2):97–114.
- Du K, Tao M, Li XB, Zhou J. Experimental study of slabbing and rockburst induced by true-triaxial unloading and local dynamic disturbance. *Rock Mech Rock Eng*. 2016;49(9):3437–3453.
- Kolsky. An investigation of the mechanical properties of materials at very high rates of loading. *Proc Phys Soc B*. 1949;62:676–700.

- 47 Li XB, Zhou ZL, Lok T-S, Hong L, Yin TB. Innovative testing technique of rock subjected to coupled static and dynamic loads. *Int J Rock Mech Min Sci.* 2008;45(5):739–748.
- 48 Zhang QB, Zhao J. A review of dynamic experimental techniques and mechanical behaviour of rock materials. *Rock Mech Rock Eng.* 2014;47(4):1411–1478.
- 49 Zhang QB, Liu K, Wu G, Zhao J. Dynamic deformation, damage, and fracture in geomaterials. In: Voyiadjis GZ, ed. *Handbook of Damage Mechanics.* 2021:1–44.
- 50 Luo Y, Wang G, Li XP, et al. Analysis of energy dissipation and crack evolution law of sandstone under impact load. *Int J Rock Mech Min Sci.* 2020:132.
- 51 Zhao J. Dynamic uniaxial compression tests on a granite. *Int J Rock Mech Min Sci.* 1999;36:273–277.
- 52 Gu H, Tao M, Li X, Cao W, Li Q. Dynamic tests and mechanical model for water-saturated soft coal with various particle gradations. *Int J Rock Mech Min Sci.* 2020;132, 104386.
- 53 Liu K, Zhao J, Wu G, Maksimenko A, Haque A, Zhang QB. Dynamic strength and failure modes of sandstone under biaxial compression. *Int J Rock Mech Min Sci.* 2020:128.
- 54 Liu K, Zhang QB, Wu G, Li JC, Zhao J. Dynamic mechanical and fracture behaviour of sandstone under multiaxial loads using a triaxial Hopkinson bar. *Rock Mech Rock Eng.* 2019;52(7):2175–2195.
- 55 Kim BH, Larson MK. *Evaluation of Bumps-Prone Potential Regarding the Spatial Characteristics of Cleat in Coal Pillars under Highly Stressed Ground Conditions. Proceedings of the 51st US Rock Mechanics/geomechanics Symposium.* American Rock Mechanics Association (ARMA); 2017.
- 56 Amadei B. Importance of anisotropy when estimating and measuring in situ stresses in rock. *Int J Rock Mech Min Sci Geomech Abstr.* 1996;33(3):293–325.
- 57 Tien YM, Kuo MC, Juang CH. An experimental investigation of the failure mechanism of simulated transversely isotropic rocks. *Int J Rock Mech Min Sci.* 2006;43(8):1163–1181.
- 58 Young RP, Nasser MHB, Sehzadeh M. Mechanical and seismic anisotropy of rocks from the ONKALO underground rock characterization facility. *Int J Rock Mech Min Sci.* 2020:126.
- 59 Jaeger JC. Shear failure of anisotropic rocks. *Geol Mag.* 2009;97(1):65–72.
- 60 Jaeger J, Cook N, Zimmerman R. *Fundamentals of Rock Mechanics.* fourth ed. London: Wiley-Blackwell; 2007.
- 61 Zhou H, Meng FZ, Zhang CQ, Hu DW, Yang FJ, Lu JJ. Analysis of rockburst mechanisms induced by structural planes in deep tunnels. *Bull Eng Geol Environ.* 2014;74(4):1435–1451.
- 62 Liu XH, Dai F, Zhang R, Liu JF. Static and dynamic uniaxial compression tests on coal rock considering the bedding directivity. *Environ Earth Sci.* 2015;73(10):5933–5949.
- 63 Tan LH, Ren T, Yang XH, He XQ. A numerical simulation study on mechanical behaviour of coal with bedding planes under coupled static and dynamic load. *Int J Mining Sci Technol.* 2018;28(5):791–797.
- 64 Yang JP, Chen WZ, Tan XJ, Yang DS. Analytical estimation of stress distribution in interbedded layers and its implication to rockburst in strong layer. *Tunn Undergr Space Technol.* 2018;81:289–295.
- 65 Hebblewhite B, Galvin J. A review of the geomechanics aspects of a double fatality coal burst at Austar Colliery in NSW, Australia in April 2014. *Int J Mining Sci Technol.* 2017;27(1):3–7.
- 66 Hagan TO, Milev AM, Spottiswoode SM, et al. Simulated rockburst experiment-an overview. *J S Afr Inst Min Metall.* 2001;101(5):217–222.
- 67 Mazaira A, Konicek P. Intense rockburst impacts in deep underground construction and their prevention. *Can Geotech J.* 2015;52(10):1426–1439.
- 68 Reddy N, Spottiswoode SM. The influence of geology on a simulated rockburst. *J S Afr Inst Min Metall.* 2001;101(5):267–272.
- 69 Manouchehrian A, Cai M. Analysis of rockburst in tunnels subjected to static and dynamic loads. *J Rock Mech Geotech Eng.* 2017;9(6):1031–1040.
- 70 He SQ, Song DZ, He XQ, et al. Coupled mechanism of compression and prying-induced rock burst in steeply inclined coal seams and principles for its prevention. *Tunn Undergr Space Technol.* 2020;98.
- 71 He SQ, Song DZ, Li ZL, et al. Mechanism and prevention of rockburst in steeply inclined and extremely thick coal seams for fully mechanized top-coal caving mining and under gob filling conditions. *Energies.* 2020;13(6).
- 72 Li J, Gong S-Y, He J, et al. Spatio-temporal assessments of rockburst hazard combining b values and seismic tomography. *Acta Geophys.* 2017;65(1):77–88.
- 73 Cao A, Dou L, Cai W, Gong S, Liu S, Jing G. Case study of seismic hazard assessment in underground coal mining using passive tomography. *Int J Rock Mech Min Sci.* 2015;78:1–9.
- 74 Liu ZG. *Rockburst Mitigating Mechanism of Hard-Roof-Blasting and its Application in the Working Face with Wide Barrier Coal Pillar of Hujirt Deep Mining Area.* PhD Thesis. Xuzhou, Jiangsu, China: China University of Mining and Technology; 2018.
- 75 ASTM-D5142. *Standard Test Methods for Proximate Analysis of the Analysis Sample of Coal and Coke by Instrumental Procedures.* 2009.
- 76 Wang S, Li X, Du K, Wang S. Experimental investigation of hard rock fragmentation using a conical pick on true triaxial test apparatus. *Tunn Undergr Space Technol.* 2018;79:210–223.
- 77 Du K, Yang C, Su R, Tao M, Wang S. Failure properties of cubic granite, marble, and sandstone specimens under true triaxial stress. *Int J Rock Mech Min Sci.* 2020:130.
- 78 Du K, Li X, Tao M, Wang S. Experimental study on acoustic emission (AE) characteristics and crack classification during rock fracture in several basic lab tests. *Int J Rock Mech Min Sci.* 2020:133.
- 79 Cadoni E, Albertini C. Modified Hopkinson bar technologies applied to the high strain rate rock tests. *Adv Rock Dyn Appl.* 2011:79–104.
- 80 Lundberg B. A split Hopkinson bar study of energy absorption in dynamic rock fragmentation. *Int J Rock Mech Min Sci Geomech Abstr.* 1976;13(6):187–197.
- 81 Garcia D, Orteu J-J, Penazzi L. A combined temporal tracking and stereo-correlation technique for accurate measurement of 3D displacements: application to sheet metal forming. *J Mater Process Technol.* 2002;125–126:736–742.
- 82 Sutton MA. Three-dimensional digital image correlation to quantify deformation and crack-opening displacement in ductile aluminum under mixed-mode I/III loading. *Opt Eng.* 2007;46(5).
- 83 Xing HZ, Zhang QB, Ruan D, Dehkhoda S, Lu GX, Zhao J. Full-field measurement and fracture characterisations of rocks under dynamic loads using high-speed three-dimensional digital image correlation. *Int J Impact Eng.* 2018;113:61–72.
- 84 Pan B, Xie H, Yang L, Wang Z. Accurate measurement of satellite antenna surface using 3D digital image correlation technique. *Strain.* 2008;45:194–200.
- 85 Zhou YX, Xia K, Li XB, et al. Suggested methods for determining the dynamic strength parameters and mode-I fracture toughness of rock materials. *Int J Rock Mech Min Sci.* 2012;49:105–112.
- 86 Li XF, Li HB, Zhang QB, Jiang JL, Zhao J. Dynamic fragmentation of rock material: characteristic size, fragment distribution and pulverization law. *Eng Fract Mech.* 2018;199:739–759.
- 87 Wen S, Zhang C, Chang Y, Hu P. Dynamic compression characteristics of layered rock mass of significant strength changes in adjacent layers. *J Rock Mech Geotech Eng.* 2020;12(2):353–365.
- 88 Ramamurthy T. Strength and modulus responses of anisotropic rocks. *Comprehen Rock Eng.* 1993;1:313–329.
- 89 Arora S, Mishra B. Investigation of the failure mode of shale rocks in biaxial and triaxial compression tests. *Int J Rock Mech Min Sci.* 2015;79:109–123.
- 90 Zhang G, Ranjith PG, Wu B, Perera MSA, Haque A, Li D. Synchrotron X-ray tomographic characterization of microstructural evolution in coal due to supercritical CO₂ injection at in-situ conditions. *Fuel.* 2019;255.
- 91 Sampath KHSM, Perera MSA, Ranjith PG, Matthai SK, Li DY. Qualitative and quantitative evaluation of the alteration of micro-fracture characteristics of supercritical CO₂-interacted coal. *J Supercrit Fluids.* 2019;147:90–101.
- 92 Weng L, Wu Z, Liu Q, Wang Z. *Energy Dissipation and Dynamic Fragmentation of Dry and Water-Saturated Siltstones under Sub-zero Temperatures.* Engineering Fracture Mechanics; 2019:220.
- 93 Tu Q, Cheng Y, Ren T, Wang Z, Lin J, Lei Y. Role of tectonic coal and gas outburst behavior during coal mining. *Rock Mech Rock Eng.* 2019;52(11):4619–4635.
- 94 Zhang QB, Zhao J. Quasi-static and dynamic fracture behaviour of rock materials: phenomena and mechanisms. *Int J Fract.* 2014;189(1):1–32.
- 95 Zhang ZX, Kou SQ, Jiang LG, Lindqvist PA. Effects of loading rate on rock fracture: fracture characteristics and energy partitioning. *Int J Rock Mech Min Sci.* 2000;37(5):745–762.
- 96 Stamboliadis ET. The energy distribution theory of comminution specific surface energy, mill efficiency and distribution mode. *Miner Eng.* 2007;20(2):140–145.
- 97 Deng Y, Chen M, Jin Y, Zou D. Theoretical analysis and experimental research on the energy dissipation of rock crushing based on fractal theory. *J Nat Gas Sci Eng.* 2016;33:231–239.
- 98 Friedman M, Handin J, Alani G. Fracture-surface energy of rocks. *Int J Rock Mech Min Sci Geomech Abstr.* 1972;9(6):757–764.
- 99 Cox SJD, Scholz CH. A direct measurement of shear fracture energy in rocks. *Geophys Res Lett.* 1985;12(12):813–816.
- 100 Mahanta B, Tripathy A, Vishal V, Singh TN, Ranjith PG. Effects of strain rate on fracture toughness and energy release rate of gas shales. *Eng Geol.* 2017;218:39–49.
- 101 Dai F, Xia K, Zheng H, Wang YX. Determination of dynamic rock Mode-I fracture parameters using cracked chevron notched semi-circular bend specimen. *Eng Fract Mech.* 2011;78(15):2633–2644.
- 102 Lockner DA, Byerlee JD, Kuksenko V, Ponomarev A, Sidorin A. Quasi-static fault growth and shear fracture energy in granite. *Nature.* 1991;350:39–42.
- 103 Lockner D. The role of acoustic emission in the study of rock fracture. *Int J Rock Mech Min Sci Geomech Abstr.* 1993;30(7):883–899.
- 104 Grosse CU, Ohtsu M. *Acoustic Emission Testing.* Heidelberg: Springer; 2008.
- 105 Ohno K, Ohtsu M. Crack classification in concrete based on acoustic emission. *Construct Build Mater.* 2010;24(12):2339–2346.
- 106 Hazzard JF, Young RP. Simulating acoustic emissions in bonded-particle models of rock. *Int J Rock Mech Min Sci.* 2000;37(5):867–872.
- 107 Ishida T, Labuz JF, Manthei G, et al. ISRM suggested method for laboratory acoustic emission monitoring. *Rock Mech Rock Eng.* 2017;50(3):665–674.